Chemie der Erde 77 (2017) 637–651

Contents lists available at ScienceDirect

Chemie der Erde

journal homepage: www.elsevier.de/chemer

SHORT COMMUNICATION

Tectonic regime switchover of Triassic Western Qinling Orogen: Constraints from LA-ICP-MS zircon U–Pb geochronology and Lu–Hf isotope of Dangchuan intrusive complex in Gansu, China

Jian-Zhen Geng[a,b], Kun-Feng Qiu[a,c,d,*], Zong-Yang Gou[a], Hao-Cheng Yu[a]

[a] State Key Laboratory of Geological Processes and Mineral Resources, China University of Geosciences, Beijing 100083, China
[b] Tianjin Institute of Geology and Mineral Resources, Tianjin 300170, China
[c] Department of Geology and Geological Engineering, Colorado School of Mines, Golden, CO 80401, USA
[d] Key Laboratory of Western Mineral Resources and Geological Engineering of Ministry of Education, Chang'an University, Xi'an 710054, China

ARTICLE INFO

Article history:
Received 10 January 2017
Received in revised form 18 May 2017
Accepted 29 May 2017
Editorial handling - Dewashish Upadhyay

Keywords:
Geochronology
Lu–Hf isotopes
Dangchuan intrusive complex
Triassic Western Qinling Orogen
Tectonic regime switchover

ABSTRACT

The Qinling Orogenic Belt, linking the Kunlun and Qilian Mountains to the west and continuing farther east to the Dabie Mountain, was assembled by the convergence and collision between the Greater South China and the North China blocks. The precise timing of the subduction and collision processes between these continental blocks and tectonic regime switchover is very equivocal. Zircon in-situ LA-ICP-MS U–Pb dating in this contribution indicates that the biotite monzogranite and monzogranite phases of the Dangchuan complex were crystallized at ca. 239.8 ± 2.3 Ma and 227.8 ± 1.2 Ma, respectively. The ca. 240 Ma biotite monzogranite displays $\varepsilon_{Hf}(t)$ values ranging from −2.4 to +2.9, and corresponding T_{DM2} of 1.72–1.94 Ga and T_{DM1} of 0.77–0.88 Ga. The ca. 228 Ma monzogranite exhibits $\varepsilon_{Hf}(t)$ values ranging from −4.3 to +1.9, and corresponding T_{DM2} of 1.73–2.08 Ga and T_{DM1} of 0.81–0.88 Ga. Lutetium–Hf isotopic composition indicates that the biotite monzogranite and monzogranite probably have the same parental magmas which were originated from hybrid sources of both reworking of Paleoproterozoic ancient crust and partial melting of the Neoproterozoic juvenile crust. The more negative $\varepsilon_{Hf}(t)$ values of the monzogranite suggest more contribution of the ancient crust during the source contamination, or more possible crustal assimilation during their crystallization at ca. 228 Ma than precursor biotite monzogranite. Integrated with previous research and our detailed petrography, we propose that the Dangchuan complex underwent an episodic growth documenting the tectonic regime switchover from early Paleozoic to Triassic. The ca. 439 Ma inherited zircon recorded the persistent subduction of the oceanic crust, the ca. 240 Ma biotite monzogranite emplaced during the northward subduction of the Mianlue oceanic crust beneath the South Qinling block, and the ca. 228 Ma monzogranite emplaced during the syn-collisional process in a compressional setting.

1. Introduction

The Qinling Orogenic Belt, linking the Kunlun and Qilian Mountains to the west and continuing farther east to the Dabie Mountain, was assembled by the convergence and collision between the South China and North China blocks (e.g., Ratschbacher et al., 2003; Dong et al., 2011; Deng et al., 2014a). It tectonically divides China into the North China block, Tarim block, South China block, and Tibetan Plateau (Zhang et al., 1995; Wang et al., 2015; Deng and Wang, 2016). The Qinling Orogenic Belt has been separated into the Western Qinling and Eastern Qinling segments (shown as blue dash line in Fig. 1B; Qiu et al., 2016b). The Western Qinling Orogen is major Triassic tectono-magmatism belt, and dozens of porphyry and skarn type copper and gold deposits associated to the extensive pulse of Early Triassic granitoids have been documented (Fig. 1B; Chen and Santosh, 2014; Qiu and Deng, 2016; Deng et al., 2017). However, the Triassic mineralization and its relationship to an evolving tectonic environment to the east of Western Qinling Orogen are still poorly understood.

Orogenic belts widely distributed around the Earth have recorded the history of plate convergence and orogenic processes (Schellart and Rawlinson, 2010; Wang et al., 2014b; Deng et al., 2015b). The granitic rocks, widespread in Western Qinling provide geodynamic constraints on the reconstruction of the convergence

* Corresponding author at: State Key Laboratory of Geological Processes and Mineral Resources, No. 29 Xueyuan Road, Haidian District, China University of Geosciences, Beijing, 100083, China.
E-mail address: kunfengqiu@qq.com (K.-F. Qiu).

http://dx.doi.org/10.1016/j.chemer.2017.05.001
0009-2819/

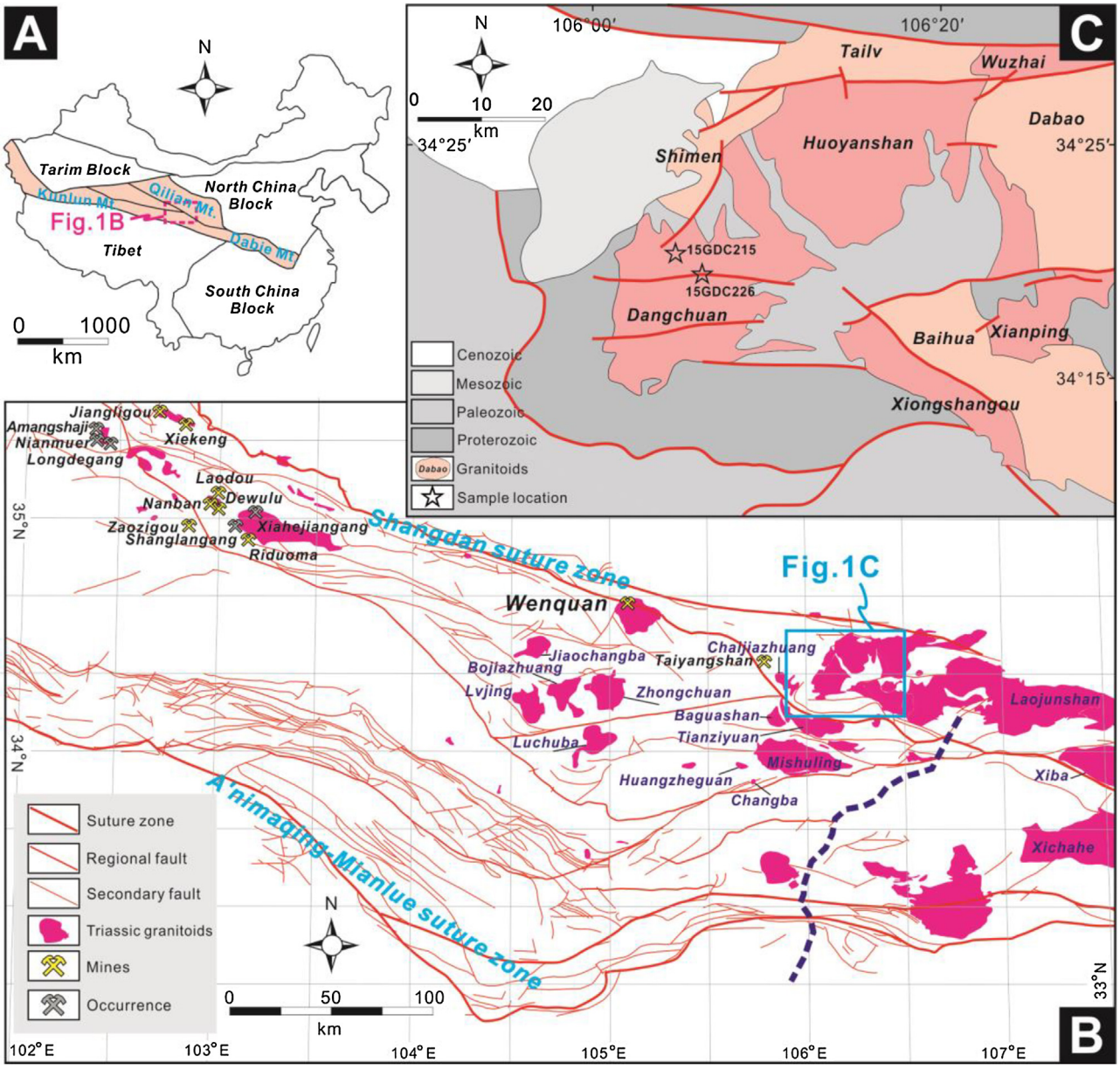

Fig. 1. (A) Tectonic subdivision of China, showing the area of the Western Qinling in this study. (B) Generalized geological map of the Western Qinling, showing the major Triassic porphyry-skarn deposits and distribution of their associated granitoids (modified after Meng and Zhang, 2000; Dong et al., 2022; Yang et al., 2015a; Qiu et al., 2015). (C) Sketch geological map of the Dangchuan area, Gansu province (Modified after Li et al., 2005; Wang et al., 2008 and our field investigation).

process of the surrounding continents. The Western Qinling and Eastern Kunlun mountains define an early Indosinian magmatism belt, and mark the site of consumption of the Paleotethys (Yan et al., 2014; Zhang et al., 2014; Li et al. (2016)). In recent years, more studies have focused on the granitic intrusions of the Qinling and its adjacent areas in order to constrain their geochronological context and petrogenesis (e.g., Jiang et al., 2010; Wang et al., 2013; Li et al., 2015a; Yang et al., 2015b), however, the precise timing, stages, and processes of the Paleozoic tectonic event as well as are poorly known (Dong et al., 2011a; Dong and Santosh, 2016; Li et al., 2017). In addition, the exact timing of the Triassic collision to the west section of the Qinling Orogen (also named Western Qinling) remains controversial and uncertain. The poorly documented research on the episodic composite intrusive complex emplacement thus hampered our holistic understanding of the tectonic evolution and geodynamic setting between these continental blocks, but also the possibility of vast potential for copper and gold mineralization likely correlated to the subduction of Paleotethys oceanic slab as well as molybdenum and gold mineralization possibly related to orogeny regionally.

The Dangchuan complex located in the eastern sector of the Western Qinling (Fig. 1B) is an ideal candidate for revealing an evolving tectonic environment in the Western Qinling. Previous research on field observations and petrology have recognized its different phases (Li et al., 2005; Wang et al., 2008; Wen et al., 2008), based on which several workers have dated them using whole-rock Rb–Sr and zircon U–Pb to determine their emplacement ages which would have tectonic implications (Table 1). Both the inconsistent ages and contradictions on their petrogenesis have introduced ambiguity for the timing and origin of the Dangchuan complex and by extension on the tectonic setting evolution of the Western Qinling orogenic segment.

Uranium–lead dating of zircon using in situ techniques has been acknowledged as the most accurate and precise dating method

Table 1
Previously published age data of the Dangchuan intrusive complex.

Sample ID	Age (Ma)	Analysed sample	Dating method	References
Tw-D1111/1	174 ± 35	Zircon	U–Pb	Li et al. (2005)
VI8	212 ± 6	Whole-rock	Rb–Sr	Li et al. (2005)
XI25	225 ± 17	Whole-rock	Rb–Sr	Li et al. (2005)
0593	220 ± 2	Zircon	LA-ICP-MS U–Pb	Wang et al. (2008)
VI48	399 ± 7	Whole-rock	Rb–Sr	Li et al. (2005)
VI49	375 ± 23	Whole-rock	Rb–Sr	Wen et al. (2008)
VI59	375 ± 6	Whole-rock	Rb–Sr	Wen et al. (2008)
VI34	391 ± 21	Whole-rock	Rb–Sr	Li et al. (2005)
0588	438 ± 3	Zircon	LA-ICP-MS U–Pb	Wang et al. (2008)

(Begemann et al., 2001). Lutetium–Hf isotope system has been broadly utilized to study the history of differentiation of the Bulk Silicate Earth due to its low concentration of initial lutetium and consequently negligible radiogenic hafnium within it (Griffin et al., 2002; Amelin and Davis, 2005). This could provide information on the formation and the crystallization age of the crust-mantle system by virtue of the fact that fractionation of lutetium from hafnium occurs during magma generation and differentiation from source rocks (Kinny and Maas, 2003).

To further promote the understanding of the convergent stages including subduction and collision processes between the North and South China blocks, we therefore in this contribution present detailed petrology, zircon in-situ LA-ICP-MS U–Pb geochronology and Lu–Hf isotopic composition of the granitoids from Dangchuan complex in the Western Qinling, with the aim of better deciphering their magma sources and geodynamic implications on precise timing of tectonic regime switchover.

2. Geologic setting

The Qinling Orogenic Belt is bounded by the Luonan-Luanchuan fault to the north and by the Mianlue suture zone to the south (Li et al., 2007a,b; Wang et al., 2013; Zhao et al., 2015; Dong et al., 2016). The Shangdan suture zone to the north separated this orogenic belt into the North Qinling and South Qinling terranes (Zhang et al., 1995; Cao et al., 2016; Li et al., 2017b). The Triassic Western Qinling Orogenic Belt is an important geological domain that separates the North and South China blocks. This belt is tectonically bounded by the North China block and Qilian Mountain Terrane to the north of the Shangdan suture zone (Fig. 1B), and A'nimaqing-Mianlue suture zone (Fig. 1B; Deng et al., 2014b; Dong et al., 2016), which defines the eastern branch of Paleotethys ocean to the south (Bian et al., 2004; Wang et al., 2014a).

The Shangdan suture resulted from the closure of the Shangdan ocean in Middle Paleozoic and the subsequent collision of the North China block and the Qinling-Dabie Microplate (Meng and Zhang, 2000; Tang et al., 2015). Following the collision, the outboard margin of this collisional orogen converted to an Andean margin (Li et al., 2017b). This suture zone comprises mélange discontinuously exposed, mainly Paleozoic ophiolitic assemblages, and subduction-related volcanic and sedimentary rocks, all intensely deformed during Paleozoic thrusting, Late Triassic sinistral ductile-shearing and Cretaceous brittle faulting (Ratschbacher et al., 2003; Li et al., 2015b). The A'nimaqing-Mainlue suture resulted from the closure of the Mianlue ocean which represents a northern branch of the eastern Paleotethyan ocean in the Middle Triassic (Liu et al., 2012; Yang et al., 2016) and ensuing collision of the Qinling-Dabie Microplate with the South China block (Meng and Zhang, 2000). The suture zone is characterized by intensively dismembered ophiolite and arc-related volcanic rocks, high-pressure/temperature metamorphic rocks, and continental-margin sedimentary rocks of Paleozoic to Middle Triassic age (Luo et al., 2012; Chen and Santosh, 2014). These were later affected by south-directed overthrusting during the Late Jurassic to Cretaceous (Dong and Santosh, 2016). The Qinling Microplate thus was trapped between the two thermally softened Andean margins related to the subduction of the Shangdan ocean and the Mianlue ocean (Li et al., 2017a).

The Triassic Western Qinling underwent a protracted and complex amalgamation process between the South China and North China blocks from Proterozoic up to late Mesozoic (Jiang et al., 2010; Dong et al., 2016). Triassic magmatism is widely expressed throughout the Paleozoic Shangdan and Triassic A'nimaqing-Mianlue suture zones Western Qinling (Wang et al., 2013; Yan et al., 2014). The Early Triassic granitoids are considered to be closely associated with the porphyry-skarn metallogenic systems (Chen and Santosh, 2014; Qiu and Deng, 2016) that are exposed to the west due to exhumation.

The Dangchuan area Gansu province is tectonically located to the northeast section of the Western Qinling (Fig. 1B), a conjunction between the Eastern Qinling, Western Qinling and North Qinling blocks. The Dangchuan area is dominantly underlain by Paleoproterozoic, early Paleozoic and Mesozoic rocks (Zhang et al., 1995). The Paleoproterozoic Qinling Group is dominated by amphibole-bearing gneiss and plagioclase-rich amphibolite and marble, and has undergone high amphibolite facies metamorphism (Li et al., 2005; Qiu et al., 2016a). The early Paleozoic Liziyuan (also named as Danfeng) Group and Caotangou (also named as Erlangping) Group mainly consist of meta- volcanic and sedimentary rocks, which expose on both sides of the Paleoproterozoic Qinling Group. The Mesozoic cover to the northwest of Dangchuan area is dominated by Cretaceous sandy conglomerate deposited in a terrestrial environment (Li et al., 2005; Wen et al., 2008). The Dangchuan complex intrudes the Qinling Group and Caotangou (Erlangping) Group had been recognized as a Paleozoic granitic complex, and subsequently acknowledged as a complex spanning early Paleozoic to early Mesozoic time, which comprises of Wuzhai, Tailv, Dabao, Shimen, Dangchuan, Huoyanshan, Baihua, Xiongshangou and xianping pluton represented dominantly by diorite and/or granite (Li et al., 2005; Wen et al., 2008; Wang et al., 2008).

3. Sampling description and analytical techniques

3.1. Sampling description

Two samples (15GDC215 and 15GDC226) were collected from the Dangchuan complex, and their localities were shown in Fig. 1C.

Biotite monzogranite is red in color, and shows a hypidiomorphic equigranular texture and massive structure (Fig. 2A). The rock is a fine- to medium-grained, and composed dominantly of alkali feldspar (30–35 vol%), plagioclase (20–30 vol%), quartz (25–28 vol%), biotite (5–8 vol%), and minor accessory minerals including magnetite, titanite, zircon and apatite (Table 2). Alkali feldspar occurs as tabular crystals and comprises microcline- and orthoclase-perthite (Fig. 3).

The monzogranite is also red in color and massive, with a fine- to medium-grained equigranular texture (Fig. 2B). The rock

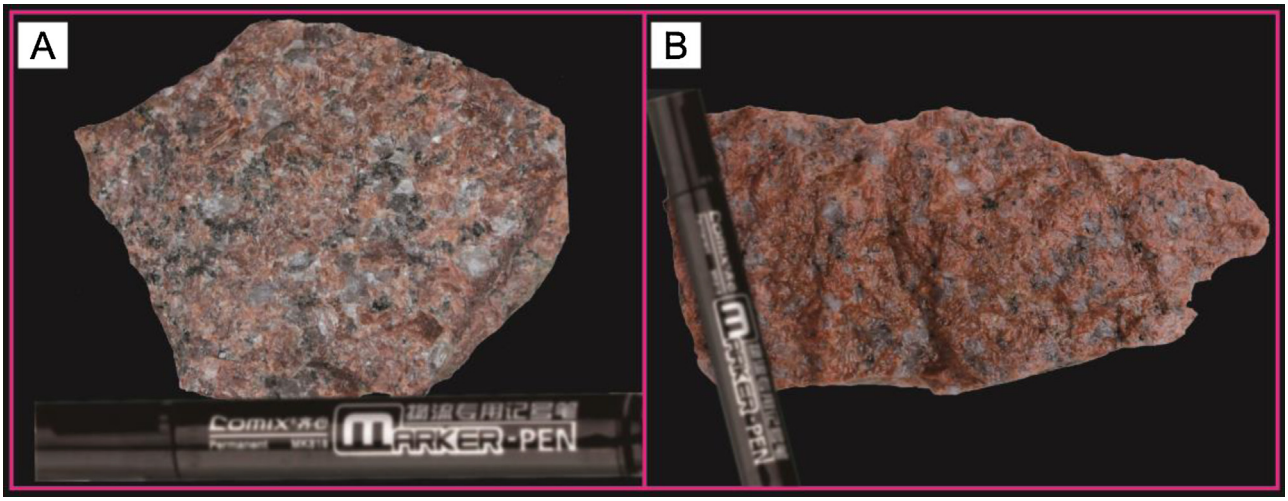

Fig. 2. Photographs of hand specimen of biotite monzogranite (A) and monzogranite (B).

Table 2
Lithology and mineralogy of the Dangchuan intrusive complex.

Lithology	Texture and structure	Mineralogy
Biotite monzogranite	Fine- to medium-grained texture; hypidiomorphic equigranular texture; massive structure.	Alkali feldspar (30–35 vol%), plagioclase (20–30 vol%), quartz (25–28 vol%), and biotite (5–8 vol%).
Monzogranite	Fine- to medium-grained texture; hypidiomorphic equigranular texture; structure.	Alkali feldspar (30–45 vol%), plagioclase (24–35 vol%), quartz (18–25 vol%), biotite (2–3 vol%), and muscovite (1–4 vol%).

is composed mainly of alkali feldspar (30–45 vol%), plagioclase (24–35 vol%), quartz (18–25 vol%), biotite (2–3 vol%), and muscovite (1–4 vol%). Magnetite, titanite, apatite and zircon are primary accessory minerals (Fig. 3).

3.2. Analytical techniques

3.2.1. Zircon mineral separation and cathodoluminescence microscopy

Zircon grains were extracted from 5 to 10 kg whole-rock samples by standard crushing, sieving, heavy liquid and magnetic separation techniques. They were mounted in epoxy blocks and polished to obtain an even surface, and then cleaned in an ultrasonic washer containing a 5% HNO_3 bath prior to laser ablationin ductively coupled plasma mass spectrometry (LA-ICP-MS) analysis. To identify the internal structure and texture of the zircon grains and to select potential positions for U–Pb analysis, cathodoluminescence (CL) images of zircons were taken on a JXA-880 electron microscope and an image analysis software was used under operating conditions of 20 kV and 20 nA, at the Institute of Mineral Resources, Chinese Academy of Geological Sciences, Beijing, China.

3.2.2. Zircon LA-ICP-MS U–Pb dating

The zircons separated from the two samples (15GDC215 and 15GDC226) of the Dangchuan complex were analyzed for U, Th, and Pb using the LA-ICP-MS facility at the Isotopic Laboratory, Tianjin Institute of Geology and Mineral Resources of China Geological Survey. Laser sampling was performed using a Neptune multiple-collector inductively coupled plasma mass spectrometer (Thermo Fisher Ltd.) to a NEW WAVE 193 nm-FX ArF Excimer laser-ablation system (ESI Ltd.). The MC-ICP-MS is a double focusing multi-collector ICP-MS. The maximum mass dispersion 17%. This machine has nine faraday cups, one fixed central channel and eight motorized Faraday cups. The SEM is bound with the central channel and the four ion counters are bound with the L4 Faraday cup. The Excimer LA system pulse width is less than 4 ns with eight different spot sizes of 2, 10, 20, 35, 50, 75, 100 and 150 μm and ablation frequency of the laser is 1–200 Hz. All analyses were conducted with a beam diameter of 30 μm, a 8 Hz repetition rate, and energy density of 11 J/cm^2. Detailed operating conditions of the laser ablation system and the MCICPMS instrument and data reduction are listed in Table 3. GJ-1 was used as an external standard for U–Pb dating analyses (published TIMS ages of $^{206}Pb/^{238}U = 600.7 \pm 1.1$ Ma, $^{207}Pb/^{235}U = 602.0 \pm 1.0$ Ma, and $^{207}Pb/^{206}Pb = 607.7 \pm 4.3$ Ma; Jackson et al., 2004). Common-Pb corrections were made using the method of Anderson (2002). NIST SRM 610 glass was used as an external standard to calculate U, Th, and Pb concentrations of zircons. Every eight analyses were followed by two analyses of the standard zircon GJ-1. $^{207}Pb/^{206}Pb$, $^{206}Pb/^{238}U$, $^{207}Pb/^{235}U$ and $^{208}Pb/^{232}Th$ ratios were calculated using ICPMSDataCal 8.4 (Liu et al., 2010). Concordia diagrams and weighted mean U–Pb ages were processed using ISOPLOT 3 (Ludwig, 2003). Age data and concordia plots were reported at 1σ error, whereas the uncertainties for weighted mean ages are given at 95% confidence level.

3.2.3. In situ zircon Lu–Hf isotope analyses

In situ zircon Hf isotopic analyses were conducted on the same spots or on the same zircon zones where U–Pb age determinations were made. Hafnium isotopic compositions were determined with a Thermo Finnigan Neptune MC-ICP-MS system coupled to a New Wave UP193 nm laser ablation system at the Laboratory of Isotope Geology, Tianjin Institute of Geology and Mineral Resources, Tianjin, China. A laser repetition rate of 11 Hz at 100 mJ was used for ablating zircons and the laser beam diameter was 50 μm. Helium was used as the carrier gas for the ablated aerosol. Details of the instrumental conditions and analytical procedures for Lu–Hf isotope analyses are shown in Table 3. Isotopes, including ^{177}Hf, ^{178}Hf, ^{179}Hf, ^{180}Hf, ^{172}Yb, ^{173}Yb, ^{175}Lu, $^{176}(Hf+Yb+Lu)$, and ^{182}W, were measured during the analytical process. Isobaric interference of

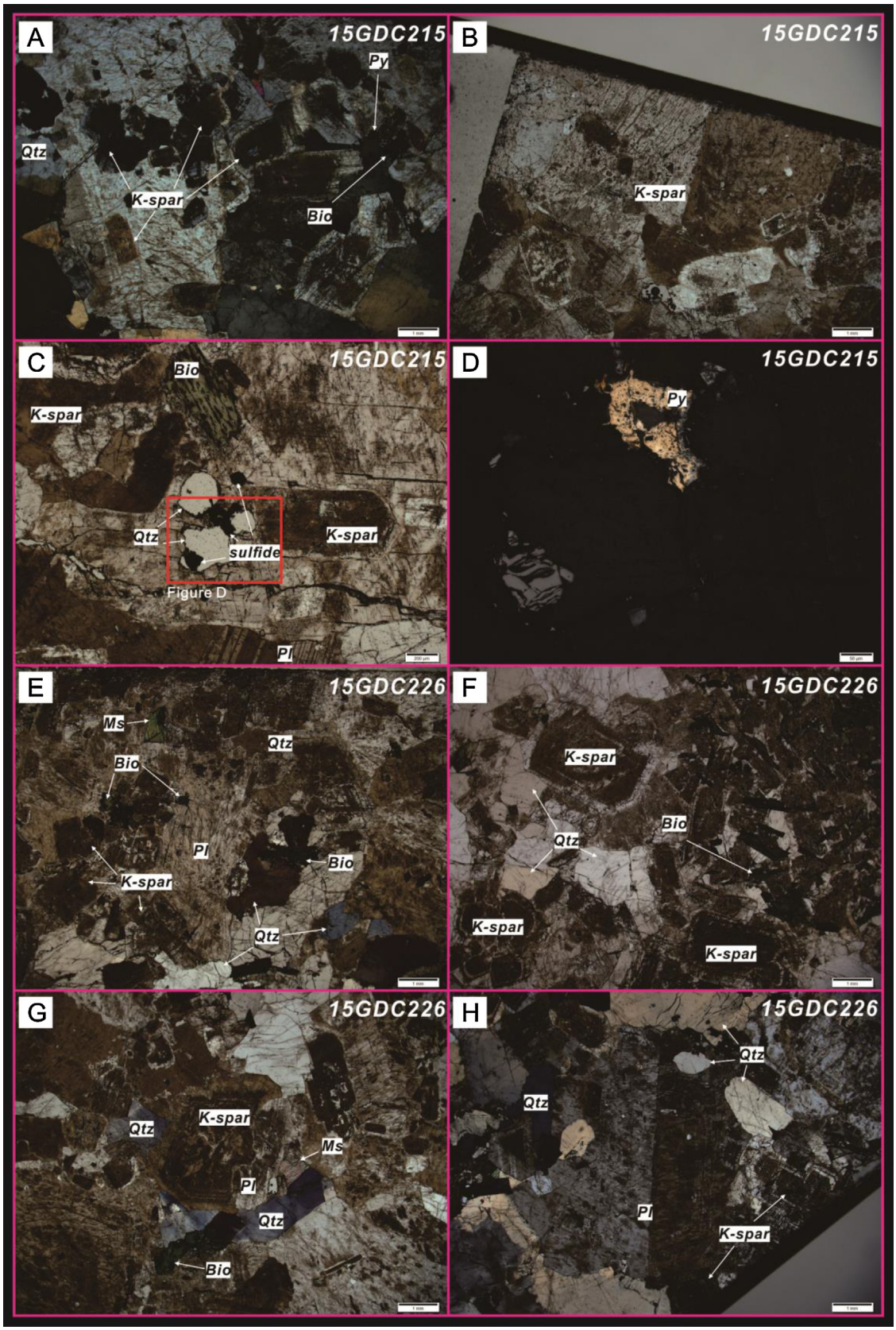

Fig. 3. Photomicrographs of biotite monzogranite (15GDC215) and monzogranite (15GDC226).

Table 3
LA-MC-ICP-MS collector configuration and operating parameters for zircon U-Pb age and Hf isotopic analysis.

L4	L3	L2	L1	C	H1	H2	H3	H4	Position of cup
^{204}Pb	^{206}Pb	^{207}Pb	^{208}Pb	219.26		^{232}Th		^{238}U	U-Pb
^{172}Yb	^{173}Yb	^{175}Lu	^{176}(Yb+Hf+Lu)	^{177}Hf	^{178}Hf	^{179}Hf	^{180}Hf	^{182}W	Hf
Parameters	U-Pb	Hf							
Cool gas(Ar)	16 L/min	16 L/min							
Auxiliary gas(Ar)	0.82 L/min	0.82 L/min							
Sample gas(Ar)	1.032 L/min	1.016L/min							
Sample gas(He)	0.86 L/min	0.82 L/min							
RF power	1200 W	1250 W							
Intergration time	0.131 s	0.131 s							
Laser enery density	10–11 J/cm^2	10–11 J/cm^2							
frequency	8 Hz	8 Hz							
beam diameter	30 μm	50 μm							

Note: L4-H4 is the number of nine Faraday Cups.

^{176}Lu on ^{176}Hf was corrected using the exponential law based on the measured ^{175}Lu value and the recommended ^{176}Lu/^{175}Lu ratio of 0.02655. Similarly, the ^{176}Yb/^{172}Yb value of 0.5887 and mean βYb value obtained during Hf analysis on the same spot were used for interference correction of ^{176}Yb mass on ^{176}Hf using the formula:

$$Hf176 = Hf_m176 - \left[Lu_m175 \times \left(\frac{Lu176}{Lu175}\right)_m \left(\frac{M_{176}}{M_{175}}\right)^{\beta(Lu)} + Yb_m172 \times \left(\frac{Yb176}{Yb172}\right)_m \left(\frac{M_{176}}{M_{172}}\right)^{\beta(Yb)}\right]$$

where

$$\beta = \ln\left(\frac{R_m}{R_t}\right) / \ln\left(\frac{M_A}{M_n}\right)$$

Where β is mass bias coefficient, *R*m is measured ratio, *R*t is true ratio, M is mass and $^{176}Hf_m = (^{176}Hf + ^{176}Yb + ^{176}Lu)_m$.

Isobaric interference corrections for Yb and Lu is importance due to the extremely low ^{176}Lu/^{177}Hf of zircons (normally <0.002), whereas the isobaric interference of ^{176}Lu is negligible during in-situ zircon Hf analyses. In this study, we use ^{173}Yb/^{172}Yb = 1.3527 and ^{173}Yb/^{172}Yb = 0.5887 to calculate both β_{Yb} and the interference of ^{176}Yb on ^{176}Hf. Because of the similar physicochemical properties of these HREEs, we use $\beta_{Lu} = \beta_{Yb}$ and ^{175}Lu/^{176}Lu = 0.02655 to calculate the interference of ^{176}Lu on ^{176}Hf. We use ^{179}Hf/^{177}Hf to calculate β_{Hf} and normalize it to 0.7325 for mass bias correction (Chu et al., 2002; Lizuka and Hirata, 2005; Wu et al., 2006).

During the analyses, the GJ-1 and 91500 zircon standards yielded ^{176}Hf/^{177}Hf ratios of 0.282008 ± 24 (2σ, n = 17) and 0.282297 ± 18 (2σ, n = 16), respectively. These ratios are all consistent with the recommended ^{176}Hf/^{177}Hf ratios of 0.282015 ± 19 (Elhlou et al., 2006) for GJ-1 and 0.282302 ± 8 (Goolaerts et al., 2004) for 91500. The decay constant for ^{176}Lu of 1.865×10^{-11} year^{-1} (Scherer et al., 2001) and present-day chondritic ratios of ^{176}Hf/^{177}Hf = 0.282785 and ^{176}Lu/^{177}Hf = 0.0336 (Blichert-Toft and Albarède, 1997) were used to calculate the $\varepsilon_{Hf}(t)$ values.

The single stage depleted-mantle model ages (T_{DM1}) were determined for each sample by calculating the intersection of the zircon/parent-rock growth trajectory with the depleted-mantle evolution curve (Vervoort and Blichert-Toft, 1999) calculated with a present-day ^{176}Hf/^{177}Hf ratio of 0.28235 (similar to MORB values) and ^{176}Lu/^{177}Hf of 0.0384. The two-stage model ages (T_{DM2}) are calculated for the source rock of the magma by projecting the initial zircon ^{176}Hf/^{177}Hf assuming a mean ^{176}Lu/^{177}Hf value of 0,009 for the upper continental crust (Griffin et al., 2002) and the average continental crustal ^{176}Lu/^{177}Hf value of 0.015. The complete formula for calculation of T_{DM1} and T_{DM2} and the assumptions are listed below:

$$(^{176}Hf/^{177}Hf)_i = (^{176}Hf/^{177}Hf)_s - (^{176}Lu/^{177}Hf)_s \times (e^{\lambda t} - 1),$$

$$\varepsilon_{Hf(0)} = ((^{176}Hf/^{177}Hf)_s/(^{176}Hf/^{177}Hf)_{CHUR,0} - 1) \times 10000,$$

$$\varepsilon_{Hf(t)} = ((^{176}Hf/^{177}Hf)_s - (^{176}Lu/^{177}Hf)_s \times (e^{\lambda t} - 1))/((^{176}Hf/^{177}Hf)_{CHUR,0} - (^{176}Lu/^{177}Hf)_{CHUR} \times (e^{\lambda t} - 1)) - 1) \times 10000,$$

$$T_{DM}1 = 1/\lambda \times Ln(1 + ((^{176}Hf/^{177}Hf)_s - (^{176}Hf/^{177}Hf)_{DM})/((^{176}Lu/^{177}Hf)_s - (^{176}Lu/^{177}Hf)_{DM})),$$

$$T_{DM2} = T_{DM1} - (T_{DM1} - t)((f_{cc} - f_s)/(f_{cc} - f_{DM1}),$$

$$f_{Lu/Hf} = (^{176}Lu/^{177}Hf)_s/(^{176}Lu/^{177}Hf)_{CHUR} - 1$$

where $(^{176}Hf/^{177}Hf)_i$ is initial ^{176}Hf/^{177}Hf, $(^{176}Hf/^{177}Hf)_s$ and $(^{176}Lu/^{177}Hf)_s$ are values of samples analyzed, and t is the crystallization time of zircon. $\lambda = 1.867 \times 10^{-11}$ (Soderlund et al., 2004) was used in the calculations. In addition, $(^{176}Hf/^{177}Hf)_{CHUR,0} = 0.282772$, $(^{176}Lu/^{177}Hf)_{CHUR} = 0.0332$ (Blichert-Toft and Albarède, 1997), and $(^{176}Hf/^{177}Hf)_{DM}$ and $(^{176}Lu/^{177}Hf)_{DM}$ of depleted mantle is 0.28325 and 0.0384, respectively (Griffin et al., 2000). f_{cc}, f_s, f_{DM} represents the $f_{Lu/Hf}$ value of continental upper crust, sample and depleted mantle, respectively.

4. Analytical results

4.1. Zircon U-Pb geochronology

The LA-ICP-MS zircon U–Pb analytical data for samples 15GDC215 and 15GDC226 are presented in Table 4 and Fig. 5. The CL images of representative analyzed zircons for U–Pb and Lu–Hf analyses are illustrated in Fig. 4.

Zircons separated from biotite monzogranite sample (sample 15GDC215) have lengths of ~150–200 μm and length/width ratios of 2:1 to 3:1. They are mostly transparent, colorless to pale yellow, and euhedral prismatic to elongated prismatic. They exhibit CL images showing concentric and typical magmatic oscillatory zoning without inherited cores, which is generally interpreted as igneous (Corfu et al., 2003). We conducted twenty-nine analyses for U–Pb ages on biotite monzogranite (sample 15GDC215),

Table 4
LA-ICP-MS zircon U–Pb dating results of the Dangchuan intrusive complex.

Sample No.	Th (ppm)	U (ppm)	Th/U	Isotopic ratios						Ages (Ma)					
				$^{207}Pb/^{206}Pb$		$^{207}Pb/^{235}U$		$^{206}Pb/^{238}U$		$^{207}Pb/^{206}Pb$		$^{207}Pb/^{235}U$		$^{206}Pb/^{238}U$	
				ratio	1σ	ratio	1σ	ratio	1σ	age	1σ	age	1σ	age	1σ
Biotite monzogranite (15GDC215) 239.8 ± 2.3 Ma (MSWD = 2.7, n = 25)															
15GDC215.1	234	413	0.57	0.0533	0.0029	0.2847	0.0148	0.0387	0.0006	344	121	254	13	245	4
15GDC215.2	2643	11956	0.22	0.0510	0.0008	0.2691	0.0076	0.0383	0.0004	239	38	242	7	242	2
15GDC215.3	321	518	0.62	0.0520	0.0014	0.2719	0.0093	0.0379	0.0004	285	63	244	8	240	3
15GDC215.4	218	414	0.53	0.0557	0.0018	0.2983	0.0122	0.0389	0.0004	439	73	265	11	246	3
15GDC215.5	166	261	0.64	0.0529	0.0023	0.2818	0.0130	0.0386	0.0005	326	98	252	12	244	3
15GDC215.6	832	2421	0.34	0.0512	0.0009	0.2653	0.0071	0.0376	0.0004	248	42	239	6	238	2
15GDC215.7	100	175	0.57	0.0583	0.0033	0.3006	0.0174	0.0374	0.0005	542	125	267	15	237	3
15GDC215.8	102	180	0.57	0.0538	0.0034	0.2870	0.0197	0.0387	0.0006	363	143	256	18	245	4
15GDC215.9	149	264	0.56	0.0528	0.0032	0.2780	0.0185	0.0382	0.0005	322	136	249	17	241	3
15GDC215.10	473	823	0.58	0.0671	0.0037	0.3285	0.0195	0.0355	0.0003	842	116	288	17	225	2
15GDC215.11	145	263	0.55	0.0578	0.0024	0.2942	0.0136	0.0369	0.0006	521	90	262	12	234	4
15GDC215.12*	277	520	0.53	0.1556	0.0043	0.5615	0.0184	0.0262	0.0003	2408	47	452	15	167	2
15GDC215.13	251	474	0.53	0.0537	0.0026	0.2721	0.0147	0.0367	0.0007	359	109	244	13	233	5
15GDC215.14	205	270	0.76	0.0538	0.0033	0.2821	0.0182	0.0381	0.0008	361	138	252	16	241	5
15GDC215.15	353	703	0.50	0.0522	0.0015	0.2663	0.0092	0.0370	0.0005	294	64	240	8	234	3
15GDC215.16*	218	319	0.68	0.0584	0.0048	0.3588	0.0197	0.0445	0.0092	547	179	311	17	281	58
15GDC215.17	355	739	0.48	0.0514	0.0014	0.2832	0.0097	0.0400	0.0006	257	63	253	9	253	4
15GDC215.18	1346	5171	0.26	0.0510	0.0009	0.2618	0.0071	0.0372	0.0006	240	41	236	6	236	3
15GDC215.19	455	831	0.55	0.0524	0.0017	0.2734	0.0102	0.0379	0.0004	301	73	245	9	240	3
15GDC215.20*	281	437	0.64	0.0610	0.0035	0.3166	0.0209	0.0377	0.0014	638	122	279	18	238	9
15GDC215.21*	165	285	0.58	0.0611	0.0038	0.3356	0.0198	0.0398	0.0021	644	134	294	17	252	13
15GDC215.22	408	859	0.47	0.0539	0.0019	0.2746	0.0125	0.0369	0.0007	368	81	246	11	234	4
15GDC215.23	452	949	0.48	0.0567	0.0022	0.3090	0.0168	0.0395	0.0005	480	84	273	15	250	3
15GDC215.24	385	772	0.50	0.0528	0.0015	0.2659	0.0089	0.0365	0.0006	320	65	239	8	231	4
15GDC215.25	366	578	0.63	0.0543	0.0020	0.2775	0.0120	0.0371	0.0005	384	81	249	11	235	3
15GDC215.26	219	509	0.43	0.0542	0.0025	0.2855	0.0135	0.0382	0.0008	380	103	255	12	242	5
15GDC215.27	196	378	0.52	0.0611	0.0063	0.3046	0.0345	0.0362	0.0006	642	222	270	31	229	4
15GDC215.28	441	738	0.60	0.0555	0.0018	0.2915	0.0142	0.0381	0.0010	434	74	260	13	241	6
15GDC215.29	298	486	0.61	0.0553	0.0027	0.2845	0.0141	0.0373	0.0011	425	111	254	13	236	7
Monzogranite (15GDC226) 227.8 ± 1.2 Ma (MSWD = 0.96, n = 21)															
15GDC226.1	117	188	0.62	0.0524	0.0018	0.2619	0.0104	0.0362	0.0004	304	77	236	9	229	3
15GDC226.2	56	76	0.73	0.0589	0.0021	0.5721	0.0235	0.0704	0.0010	564	79	459	19	439	6
15GDC226.3	60	121	0.49	0.0564	0.0030	0.2866	0.0154	0.0369	0.0005	467	116	256	14	233	3
15GDC226.4	61	109	0.56	0.0542	0.0020	0.2789	0.0122	0.0373	0.0004	379	82	250	11	236	3
15GDC226.5	100	137	0.73	0.0537	0.0040	0.2724	0.0196	0.0368	0.0008	359	169	245	18	233	5
15GDC226.6	168	221	0.76	0.0523	0.0020	0.2576	0.0107	0.0357	0.0004	297	86	233	10	226	2
15GDC226.7*	53	96	0.55	0.1730	0.0063	0.9850	0.0392	0.0413	0.0006	2587	61	696	28	261	4
15GDC226.8	101	190	0.53	0.0583	0.0055	0.2879	0.0269	0.0358	0.0004	540	206	257	24	227	3
15GDC226.9	42	100	0.42	0.0510	0.0039	0.2634	0.0255	0.0375	0.0006	241	178	237	23	237	4
15GDC226.10	108	181	0.60	0.0550	0.0024	0.2892	0.0138	0.0381	0.0006	413	97	258	12	241	4
15GDC226.11	58	124	0.47	0.0546	0.0024	0.2872	0.0140	0.0382	0.0005	394	101	256	12	242	3
15GDC226.12	94	191	0.49	0.0572	0.0034	0.2956	0.0174	0.0375	0.0007	500	133	263	15	237	4
15GDC226.13	141	251	0.56	0.0555	0.0025	0.2925	0.0135	0.0382	0.0004	434	99	260	12	242	3
15GDC226.14	341	683	0.50	0.0545	0.0014	0.2723	0.0085	0.0362	0.0005	392	58	245	8	229	3
15GDC226.15	267	516	0.52	0.0547	0.0010	0.2987	0.0076	0.0396	0.0004	399	42	265	7	251	2
15GDC226.16*	329	723	0.45	0.0594	0.0014	0.3078	0.0099	0.0376	0.0022	581	51	272	9	238	14
15GDC226.17*	235	425	0.55	0.1547	0.0048	0.9220	0.0322	0.0432	0.0004	2399	52	663	23	273	3
15GDC226.18	92	217	0.42	0.0492	0.0025	0.2511	0.0140	0.0370	0.0004	158	120	227	13	234	2
15GDC226.19	116	171	0.68	0.0500	0.0042	0.2577	0.0212	0.0374	0.0008	194	194	233	19	237	5
15GDC226.20	427	502	0.85	0.0506	0.0009	0.2547	0.0065	0.0365	0.0004	222	43	230	6	231	3
15GDC226.21	216	461	0.47	0.0529	0.0014	0.2643	0.0081	0.0362	0.0004	326	62	238	7	229	2
15GDC226.22	166	309	0.54	0.0541	0.0033	0.2752	0.0177	0.0369	0.0005	374	136	247	16	234	3
15GDC226.23	187	268	0.70	0.0527	0.0015	0.2627	0.0088	0.0362	0.0004	314	66	237	8	229	2
15GDC226.24*	261	457	0.57	0.3882	0.0090	3.1884	0.1262	0.0596	0.0011	3864	35	1454	58	373	7
15GDC226.25	66	154	0.43	0.0503	0.0051	0.2561	0.0256	0.0369	0.0004	210	236	232	23	234	3

Note: Data marked with * are excluded while being calculated due to their discordance.

four analyses (samples 15GDC215.12, 15GDC215.16, 15GDC215.20 and 15GDC215.21) among which are excluded because they are statistical outliers. Results of remaining twenty-five analyses have 175–11956 ppm U, 100–2643 ppm Th, and Th/U ratios are between 0.22 and 0.76, suggesting that they are of magmatic origin (Belousova et al., 2006). All of these data are concordant and yield a weighted mean age of 239.8 ± 2.3 Ma (MSWD = 2.7, n = 25).

For the monzogranite sample (15GDC226), twenty-five analyses were carried out for U–Pb age dating, among which, four analyses (samples 15GDC226.7, 15GDC226.16, 15GDC226.17 and 15GDC226.24) are excluded because they are statistical outliers. Twenty analyses out of the remaining twenty-one analyses on zircons from monzogranite (15GDC226) have concordant $^{206}Pb/^{238}U$ and $^{207}Pb/^{235}U$ ratios within the analytical precision (Fig. 5), yielding a weighted average age of 227.8 ± 1.2 Ma (MSWD = 0.96, n = 20). These zircons are colorless, transparent and euhedral, and most are short to long prismatic, with length-to-width ratios between 1:1 and 3:1. They have CL images displaying broad and concentric oscillatory zones, and 100–683 ppm U, 42–427 ppm Th, and Th/U ratios ranging from 0.42 to 0.85. One additional zircon

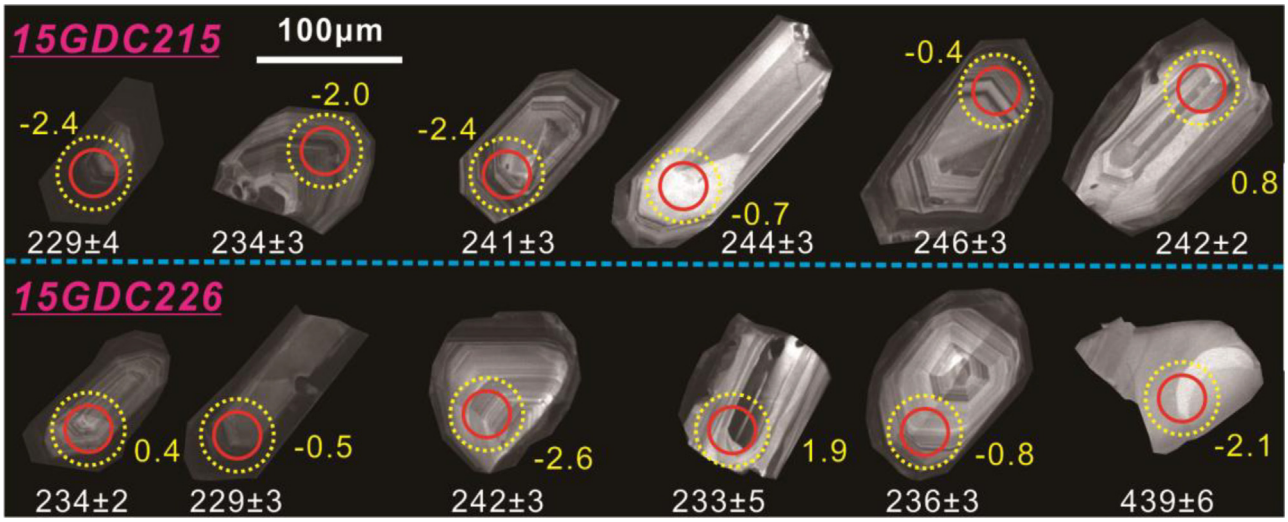

Fig. 4. Representative CL images of zircons derived from 15GDC215 and 15GDC226 with identified analytical spot, U–Pb age (Ma) and $\varepsilon_{Hf}(t)$ value. Red circle: U–Pb beam. Yellow dash circle: Hf beam. (For interpretation of the references to color in this figure legend, the reader is referred to the web version of this article.)

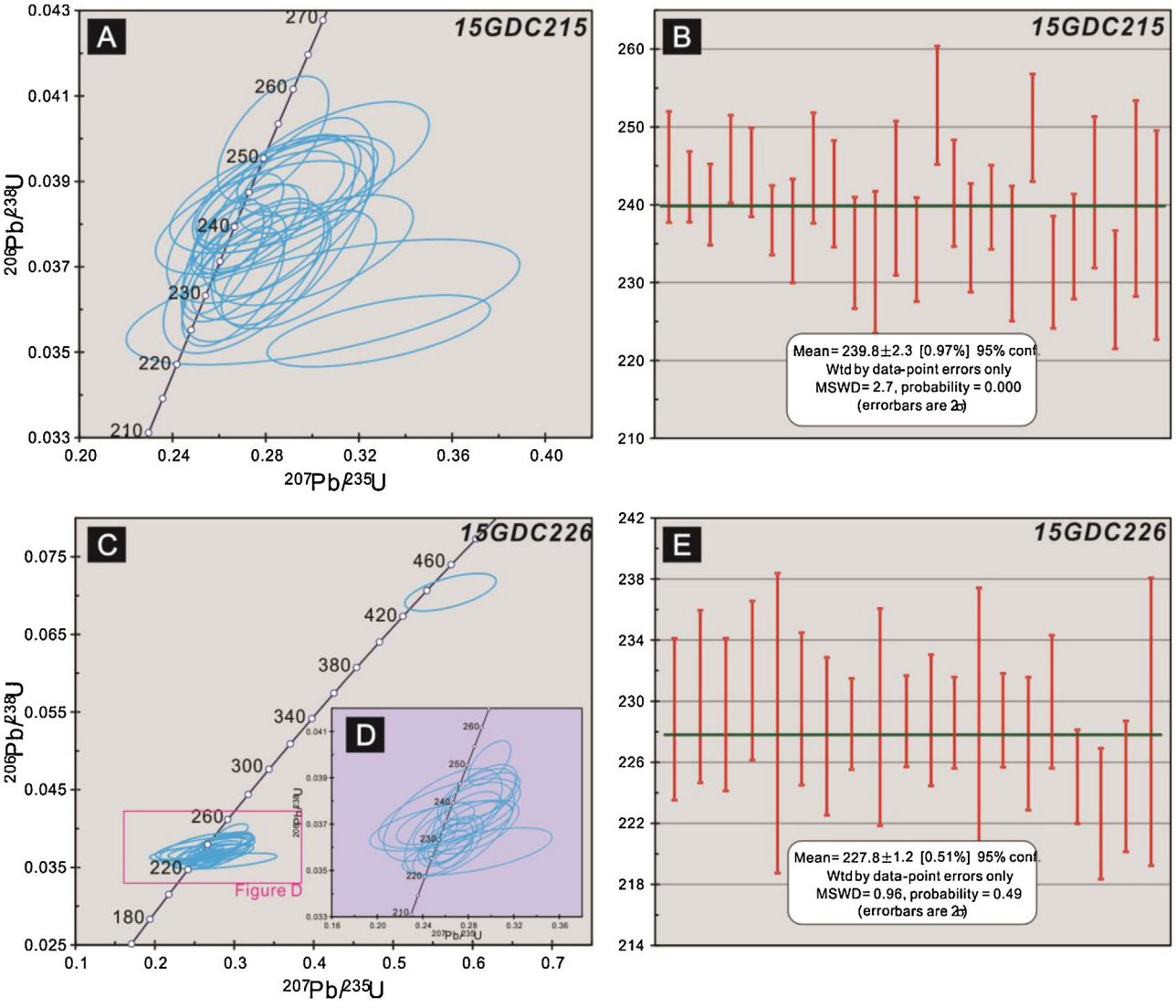

Fig. 5. LA-ICP-MS zircon U–Pb concordia diagrams for 15GDC215 (A, B) and 15GDC226 (C, D, E), respectively.

exhibits an anomalously old $^{206}Pb/^{238}U$ age at 439 ± 6 Ma. This zircon displays no concentric oscillatory zones (Fig. 4), and relatively lower Th (56 ppm) and U (76 ppm) concentrations than those of 227.8 ± 1.2 Ma group of zircons.

4.2. Zircon Lu-Hf isotopic composition

Zircon Lu–Hf isotopic data are presented in Table 5, and shown in Fig. 6. Hafnium isotopic data, expressed as values of epsilon Hf ($\varepsilon_{Hf}(t)$) at the time of formation, from the biotite monzogranite and monzogranite are plotted versus time in Fig. 6.

For biotite monzogranite (sample 15GDC215), the twenty-five analyses have low ratios of $^{176}Lu/^{177}Hf$ = 0.000615–0.002425, indicating very little radiogenic Hf. Thus the measured $^{176}Hf/^{177}Hf$ ratios (0.282663–0.282711) can approximately represent initial Hf isotopic composition. They display $\varepsilon_{Hf}(t)$ values ranging from −2.4 to +2.9, with an average of −0.2, among which, sixteen analyses yielding negative $\varepsilon_{Hf}(t)$ values have corresponding T_{DM2} of 1.72–1.94 Ga, and nine analyses yielding positive $\varepsilon_{Hf}(t)$ values have corresponding T_{DM1} of 0.77–0.88 Ga.

We made twenty-one Lu–Hf isotopic analyses on the same spots that were used to determine U–Pb ages of monzogranite (sample 15GDC226). They have very low $^{176}Lu/^{177}Hf$ ratios, indicating very little radiogenic Hf. The measured $^{176}Hf/^{177}Hf$ ratios thus approximately represent initial Hf isotopic composition (age corrected using U–Pb age for individual grain). One zircon with age of ~439 Ma has $^{176}Lu/^{177}Hf$ ratio of 0.000576, $^{176}Hf/^{177}Hf$ ratios of 0.282446, and negative $\varepsilon_{Hf}(t)$ value of −2.1 with corresponding T_{DM2} of 2.02 Ga. The dominant twenty analyses for an estimated age at ca. 228 Ma have ratios of $^{176}Lu/^{177}Hf$ = 0.000627–0.001756 and $^{176}Hf/^{177}Hf$ = 0.282509–0.282686. They display $\varepsilon_{Hf}(t)$ values ranging from −4.3 to +1.9, with an average of −0.8, among which, thirteen analyses yielding negative $\varepsilon_{Hf}(t)$ values have corresponding T_{DM2} of 1.73–2.08 Ga, and seven analyses yielding positive $\varepsilon_{Hf}(t)$ values have corresponding T_{DM1} of 0.81–0.88 Ga.

5. Discussion

5.1. Episodic growth of the Dangchuan complex

The emplacement age of the Dangchuan complex has been long debated. Li et al. (2005) initially conducted Rb-Sr dating on whole-rock, and reported the ages of composite Dangchuan complex of 391 ± 21 Ma, 399 ± 7 Ma, 225 ± 17 Ma, and 212 ± 6 Ma. These ages indicate that the Dangchuan complex possibly underwent pulsed emplacement at ca. 390 Ma, 225 Ma, and 212 Ma, which however, was contradictory to their subsequent zircon U–Pb dating at 174 ± 35 Ma (Li et al., 2005). Wen et al. (2008) subsequently carried out Rb-Sr dating on whole-rock and reported ages of 375 ± 23 Ma and 375 ± 6 Ma, due to which the Dangchuan complex was proposed to be single magmatism corresponding to the evolution of the Mianlue ocean. Although Wang et al. (2008) further documented new ages at 438 ± 3 Ma and 220 ± 2 Ma by using LA-ICP-MS zircon U–Pb dating approach based on detailed field observations showing different phases of the Dangchuan complex, the accurate and holistic episodic growth of the Dangchuan complex still remained still a key problem. This accurate and precise geochronology in this study of the Dangchuan complex located in the North Qinling block provides constraints on tectonic implications during Paleozoic to Mesozoic of the Qinling orogeny.

Robust LA-ICP-MS zircon U–Pb ages in this contribution record the time of emplacement of biotite monzogranite at 239.8 ± 2.3 Ma, and monzogranite at 227.8 ± 1.2 Ma (Fig. 5) of the composite Dangchuan complex. This is consistent to that of widespread Triassic magmatism in Western Qinling (Fig. 1B). One zircon from monzogranite yields a $^{206}Pb/^{238}U$ age of 439 ± 6 Ma (Fig. 5), closely consistent with the emplacement age of Dangchuan complex previously documented by robust LA-ICP-MS zircon U–Pb method (Sample 0588: 438 ± 3 Ma; Wang et al., 2008). This indicates that this zircon could be inherited from a precusor phase at ca. 439 Ma of the Dangchuan complex during magma crystallization at ca. 228 Ma. This Paleozoic magmatism is consistent with sixteen plutons with ages of 460–422 Ma ("The second-stage granitoids"; Wang et al., 2013) intruding the Yaolinghe and Wudang groups in the South Qinling block, the other plutons emplaced in the Qinling Complex, and Erlangping, Danfeng and Kuanping groups in the North Qinling block (Yu et al., 2015; Dong and Santosh, 2016; Tang et al., 2016). Integrated our field and petrological observation with geochronology data in this study, we there propose that the Dangchuan complex records an episodic magma growth starting from ca. 240 Ma till ca. 228 Ma. The ca. 439 Ma inherited zircon which is consistent to previous geochronological data of 438 ± 3 Ma reported by Wang et al. (2008) and regional ca. 460–422 Ma population magmatism possibly indicates an early Paleozoic magmatic event.

5.2. Petrogenesis of Triassic granitoids

Lutetium–hafnium isotopic composition of zircons is a very sensitive geochemical tracer to detect the evolutionary history of the crustal and mantle material (Blichert-Toft and Albarède, 1997). Hafnium is partitioned more strongly into melts than Lu during partial melting, the crust therefore generally has lower $^{176}Lu/^{177}Hf$ and $^{176}Hf/^{177}Hf$ ratios than the mantle. Accordingly, granitoids displaying positive $\varepsilon_{Hf}(t)$ values are considered to be sourced from the partial melting of juvenile crustal materials, while the negative $\varepsilon_{Hf}(t)$ values indicate a source of old crust. The ca. 240 Ma biotite monzogranite (sample 15GDC215) yields relatively lower ratios of $^{176}Lu/^{177}Hf$ = 0.000615–0.002425 and $^{176}Hf/^{177}Hf$ = 0.282663–0.282711, and $\varepsilon_{Hf}(t)$ values ranging from −2.4 to +2.9 up to five epsilon units possessing heterogeneous zircon Hf isotopic compositions. These samples plot on the chondrite uniform reservoir (CHUR) line (Fig. 6A). The sixteen analyses with negative $\varepsilon_{Hf}(t)$ values have corresponding T_{DM2} of 1.72–1.94 Ga, and nine analyses with positive $\varepsilon_{Hf}(t)$ values have corresponding T_{DM1} of 0.77–0.88 Ga (Fig. 6C). In contrast, the ca. 228 Ma monzogranite displays $\varepsilon_{Hf}(t)$ values ranging from −4.3 to +1.9, up to six epsilon units (Fig. 6A), indicating more negative but less positive zircon Hf isotopic compositions than that of precursor biotite monzogranite. This indicates that their magma sources could be relatively heterogeneous than that of ca. 240 Ma biotite monzogranite. The 13 analyses with negative $\varepsilon_{Hf}(t)$ values have corresponding T_{DM2} of 1.73–2.08 Ga, and seven analyses yielding positive $\varepsilon_{Hf}(t)$ values have corresponding T_{DM1} of 0.81–0.88 Ga (Fig. 6C).

During partial melting, the once uniform mantle would produce Lu/Hf fractionation with formation of basaltic magma (low Lu/Hf) and mantle residue (high Lu/Hf). Consequently, the residual and depleted mantle, which has Lu/Hf > chondrites, will be progressively radiogenic with positive $\varepsilon_{Hf}(t)$ values. In contrast, the enriched ancient crust, with Lu/Hf < chondrites, will be non-radiogenic with negative $\varepsilon_{Hf}(t)$ values (Kinny and Maas, 2003). The biotite monzogranite and monzogranite both dominantly fall within the area on the evolutionary trend line of the Archean continental crust. They moreover show positive $\varepsilon_{Hf}(t)$ values, but much lower than that of depleted mantle, indicating that their magmas were derived from juvenile crust. Thus the zircons that have low positive $\varepsilon_{Hf}(t)$ values rule out the involvement of a mantle source in their magma genesis. The positive $\varepsilon_{Hf}(t)$ values indicate that they could be sourced from the partial melting of juvenile crustal materials, while the negative $\varepsilon_{Hf}(t)$ values indicate their source of ancient

Table 5
In situ zircon Lu–Hf isotopic composition of the Dangchuan intrusive complex.

Sample No.	Age (Ma)	$^{176}Yb/^{177}Hf$	2σ	$^{176}Lu/^{177}Hf$	2σ	$^{176}Hf/^{177}Hf$	2σ	$\varepsilon_{Hf}(0)$	$\varepsilon_{Hf}(t)$	T_{DM1} (Ma)	T_{DM2} (Ma)	$f_{Lu/Hf}$
Biotite monzogranite (15GDC215) 239.8 ± 2.3 Ma												
15GDG215.1	245	0.035846	0.000796	0.001062	0.000017	0.282621	0.000020	−5.4	−0.2	896	1715	−0.97
15GDC215.2	242	0.080875	0.000280	0.002425	0.000009	0.282655	0.000020	−4.1	0.8	880	1628	−0.93
15GDC215.3	240	0.029411	0.000239	0.000945	0.000003	0.282589	0.000018	−6.5	−1.3	937	1818	−0.97
15GDC215.4	246	0.031103	0.000349	0.000968	0.000015	0.282613	0.000017	−5.6	−0.4	905	1736	−0.97
15GDC215.5	244	0.025054	0.000120	0.000781	0.000005	0.282603	0.000021	−6.0	−0.7	914	1767	−0.98
15GDC215.6	238	0.030444	0.000739	0.000983	0.000022	0.282587	0.000015	−6.6	−1.5	942	1830	−0.97
15GDC215.7	237	0.023812	0.000057	0.000758	0.000002	0.282611	0.000023	−5.7	−0.6	903	1752	−0.98
15GDC215.8	245	0.024996	0.000561	0.000761	0.000016	0.282629	0.000021	−5.1	0.2	877	1683	−0.98
15GDC215.9	241	0.026220	0.000224	0.000846	0.000009	0.282558	0.000021	−7.6	−2.4	979	1915	−0.97
15GDC215.10	225	0.028701	0.000936	0.000853	0.000028	0.282612	0.000023	−5.7	−0.9	904	1765	−0.97
15GDC215.11	234	0.019773	0.000649	0.000615	0.000018	0.282663	0.000022	−3.9	1.2	827	1589	−0.98
15GDC215.12*	167	0.020989	0.000156	0.000679	0.000001	0.282579	0.000020	−6.8	−3.3	946	1943	−0.98
15GDC215.13	233	0.024409	0.000254	0.000787	0.000010	0.282596	0.000020	−6.2	−1.2	925	1805	−0.98
15GDC215.14	241	0.020789	0.000118	0.000686	0.000002	0.282665	0.000019	−3.8	1.4	825	1572	−0.98
15GDC215.15	234	0.034551	0.000114	0.001124	0.000001	0.282576	0.000019	−6.9	−2.0	961	1871	−0.97
15GDC215.16*	281	0.038976	0.001204	0.001193	0.000035	0.282627	0.000019	−5.1	0.8	890	1651	−0.96
15GDC215.17	253	0.042349	0.000344	0.001254	0.000006	0.282603	0.000022	−6.0	−0.6	926	1764	−0.96
15GDC215.18	236	0.039623	0.000296	0.001199	0.000007	0.282606	0.000020	−5.9	−0.9	920	1774	−0.96
15GDC215.19	240	0.035123	0.000233	0.001079	0.000007	0.282611	0.000018	−5.7	−0.6	910	1751	−0.97
15GDC215.20*	238	0.037274	0.000255	0.001124	0.000016	0.282602	0.000021	−6.0	−1.0	925	1784	−0.97
15GDC215.21*	252	0.042871	0.000606	0.001293	0.000023	0.282628	0.000021	−5.1	0.2	892	1686	−0.96
15GDC215.22	234	0.037459	0.000389	0.001115	0.000001	0.282621	0.000022	−5.3	−0.4	897	1727	−0.97
15GDC215.23	250	0.044187	0.000850	0.001284	0.000020	0.282671	0.000023	−3.6	1.7	831	1552	−0.96
15GDC215.24	231	0.025381	0.000240	0.000756	0.000004	0.282568	0.000022	−7.2	−2.2	962	1893	−0.98
15GDC215.25	235	0.029241	0.000235	0.000869	0.000007	0.282680	0.000021	−3.2	1.8	808	1534	−0.97
15GDC215.26	242	0.044351	0.000718	0.001267	0.000013	0.282695	0.000025	−2.7	2.4	796	1486	−0.96
15GDC215.27	229	0.033725	0.000079	0.001096	0.000001	0.282654	0.000020	−4.2	0.7	851	1630	−0.97
15GDC215.28	241	0.044905	0.000603	0.001310	0.000012	0.282711	0.000028	−2.2	2.9	774	1435	−0.96
15GDC215.29	236	0.042612	0.000264	0.001403	0.000018	0.282568	0.000022	−7.2	−2.3	980	1898	−0.96
Monzogranite (15GDC226) 227.8 ± 1.2 Ma												
15GDC226.1	229	0.039053	0.000105	0.001217	0.000002	0.282585	0.000027	−6.6	−1.8	950	1849	−0.96
15GDC226.2	439	0.017201	0.000417	0.000576	0.000013	0.282446	0.000019	−11.5	−2.1	1128	2015	−0.98
15GDC226.3	233	0.029677	0.000069	0.000929	0.000001	0.282531	0.000020	−8.5	−3.5	1019	2012	−0.97
15GDC226.4	236	0.028918	0.000075	0.000870	0.000003	0.282607	0.000022	−5.8	−0.8	910	1765	−0.97
15GDC226.5	233	0.037339	0.000452	0.001117	0.000012	0.282686	0.000024	−3.0	1.9	805	1521	−0.97
15GDC226.6	226	0.042843	0.000282	0.001304	0.000005	0.282675	0.000025	−3.4	1.3	825	1567	−0.96
15GDC226.7*	261	0.027524	0.000069	0.000869	0.000004	0.282564	0.000020	−7.3	−1.8	971	1871	−0.97
15GDC226.8	227	0.037198	0.000878	0.001276	0.000021	0.282622	0.000019	−5.3	−0.5	899	1735	−0.96
15GDC226.9	237	0.034958	0.000086	0.001076	0.000003	0.282630	0.000019	−5.0	0.0	883	1695	−0.97
15GDC226.10	241	0.035068	0.000346	0.001052	0.000007	0.282616	0.000021	−5.5	−0.4	903	1735	−0.97
15GDC226.11	242	0.020088	0.000024	0.000627	0.000001	0.282550	0.000018	−7.8	−2.6	984	1936	−0.98
15GDC226.12	237	0.031672	0.000178	0.001016	0.000005	0.282540	0.000017	−8.2	−3.2	1009	1980	−0.97
15GDC226.13	242	0.060785	0.002365	0.001708	0.000064	0.282509	0.000022	−9.3	−4.3	1072	2084	−0.95
15GDC226.14	229	0.036885	0.000152	0.001398	0.000006	0.282621	0.000021	−5.4	−0.5	905	1739	−0.96
15GDC226.15	251	0.036990	0.000090	0.001147	0.000001	0.282572	0.000017	−7.1	−1.8	967	1863	−0.97
15GDC226.16*	238	0.037646	0.000407	0.001206	0.000013	0.282604	0.000016	−6.0	−0.9	924	1779	−0.96
15GDC226.17*	273	0.042114	0.002211	0.001238	0.000066	0.282532	0.000019	−8.5	−2.7	1026	1964	−0.96
15GDC226.18	234	0.042058	0.001060	0.001314	0.000031	0.282643	0.000019	−4.5	0.4	870	1659	−0.96
15GDC226.19	237	0.024163	0.000099	0.000766	0.000004	0.282617	0.000023	−5.5	−0.4	895	1733	−0.98
15GDC226.20	231	0.049810	0.000451	0.001565	0.000018	0.282603	0.000019	−6.0	−1.1	934	1794	−0.95
15GDC226.21	229	0.038666	0.000353	0.001160	0.000007	0.282643	0.000023	−4.6	0.3	867	1664	−0.97
15GDC226.22	234	0.032759	0.000171	0.000987	0.000006	0.282678	0.000020	−3.3	1.7	813	1544	−0.97
15GDC226.23	229	0.045260	0.000387	0.001756	0.000020	0.282582	0.000022	−6.7	−2.0	969	1868	−0.95
15GDC226.24*	373	0.033746	0.000616	0.001075	0.000024	0.282549	0.000021	−7.9	0.0	998	1781	−0.97
15GDC226.25	234	0.031008	0.000276	0.000941	0.000003	0.282656	0.000022	−4.1	0.9	844	1615	−0.97

Note: Data marked with * are excluded while being calculated due to their discordance.

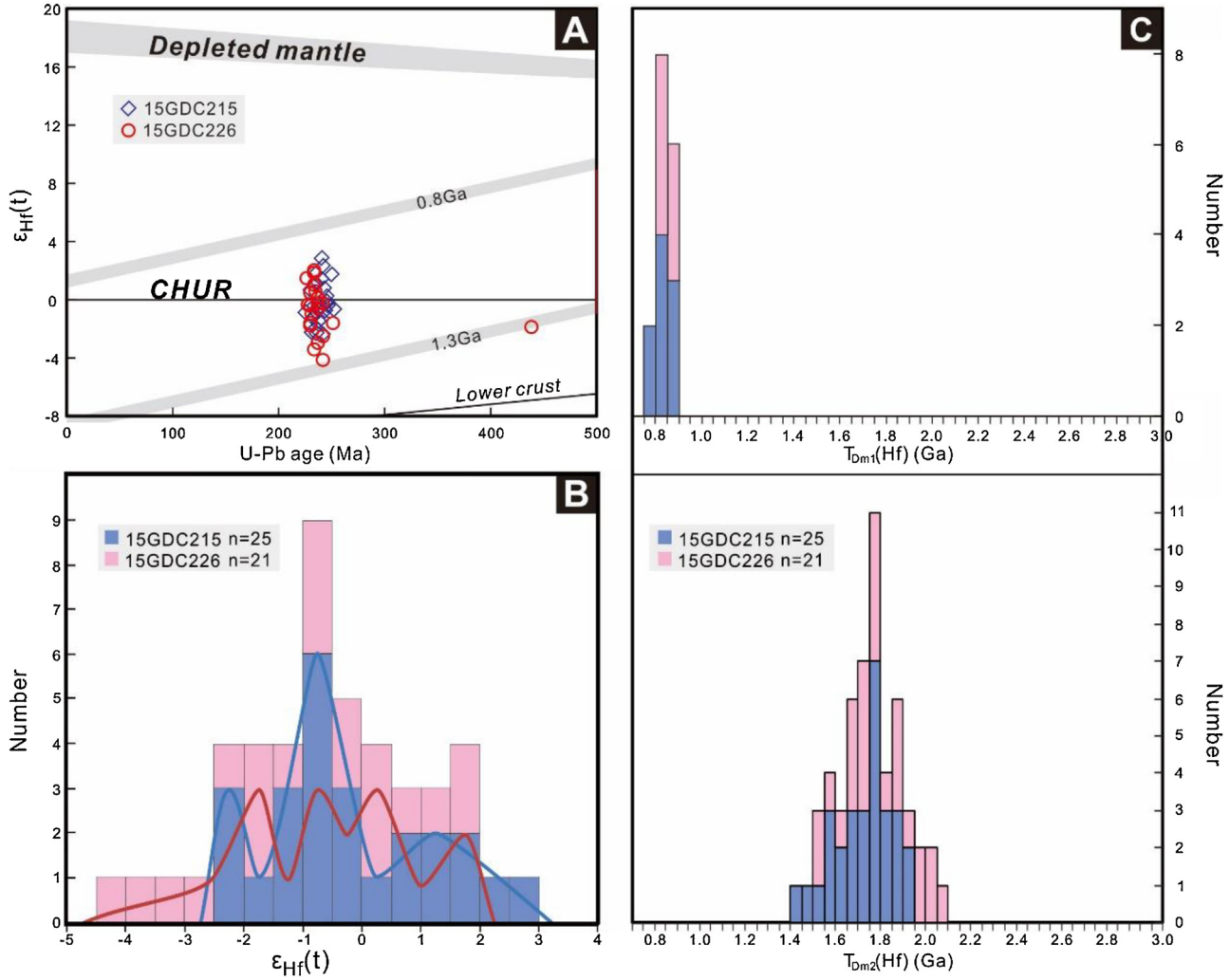

Fig. 6. Lutetium–Hf isotopic composition of zircons from 15GDC215 and 15GDC226. (A) Variations of $\varepsilon_{Hf}(t)$ values versus U–Pb ages (Ma). (B) Histograms and frequency curves of $\varepsilon_{Hf}(t)$ values. (C) Histograms of corresponding T_{DM1} and T_{DM2} (Ga) of zircons with positive and negative $\varepsilon_{Hf}(t)$ values, respectively.

crust. However, mixing with an undepleted or enriched source, for example, by crustal contamination, has also been considered to result in low positive as zircons from biotite monzogranite and monzogranite in this study, zero, or negative $\varepsilon_{Hf}(t)$ during their crystallization (Kinny and Maas, 2003). Low positive $\varepsilon_{Hf}(t)$ values have generally been interpreted as indicating crustal contamination (Corfu and Stott, 1993). This is consistent with existence of the ca. 439 Ma inherited zircon which yielding negative $\varepsilon_{Hf}(t)$ value of −2.1 with corresponding T_{DM2} of 2.02 Ga in the ca. 228 Ma monzogranite, and their more negative $\varepsilon_{Hf}(t)$ values (Fig. 6A), suggesting an evolved felsic magma with several inherited components. We argued that the ca. 240 Ma biotite monzogranite and ca. 228 Ma monzogranite could be possibly mixed in their source itself or were assimilated at a deep crustal level or some part reflects contamination from wall rocks when intruded into the Triassic orogenic system

This conclusion is consistent to that derived from previous petrogeochemical data of contemporaneous igneous rocks regionally. Li et al. (2007a,b) preliminarily reported whole-rock petrogeochemistry of Silurian and post-Devonian granitoids of the Dangchuan intrusive complex. The ca. 250–235 Ma magmatism coeval with biotite monzogranite in this study is widespread throughout Western Qinling, including Xiahe, Yeliguan, Tongren granodiorite, Dewulu quartz diorite and mafic enclave, Meiwu granodiorite, biotite granite and mafic enclave, Jiangligou biotite, Shuangpengxi granodiorite, Xiekeng gabbro diorite, Shehaliji quartz monzonite (Luo et al., 2012; Yan et al., 2014; Qiu and Deng, 2016; and references therein). This belt together with Eastern Kunlun developing broadly coeval early Indosinian magmatism defines a regionally similar geodynamic process related to the Paleotethys ocean and marks the consumption of the Paleotethys ocean at ca. 234 Ma by northward subduction (Yan et al., 2014; Zhang et al., 2014; Wang et al., 2016a,b; Qiu et al., 2016a). They display characteristics of metaluminous and calc-alkaline to high-K calc-alkaline, and show affinity of I-type granites, and are dominantly enriched in LREEs, and Rb, U and Th, depleted in HREEs and Ba, Sr, Nb and Ta, and characterized by negative Eu anomalies. This indicates their affinity to island-arc granites related to the extension of Paleotethys ocean basin during Late Permian to Early Triassic, and further constrains the northward subduction of Paleotethys ocean lasting until ca. 234 Ma.

The ca. 228–190 Ma granitoids prevailing in Western Qinling are geodynamically associated with collision between the North China and South China blocks, and are further grouped into syn-collision granitoids with ages of 228–215 Ma and post-collision granitoids with ages of ca. 215–190 Ma (Jiang et al., 2010; Wang et al., 2013; Li et al., 2015a; Qiu et al., 2016b). The ca. 228–215 Ma granitoids coeval with monzogranite in this study comprise quartz diorites, quartz monzonites, granodiorites, and monzogranites, and display dominatedly metaluminous to slightly peraluminous and high-K

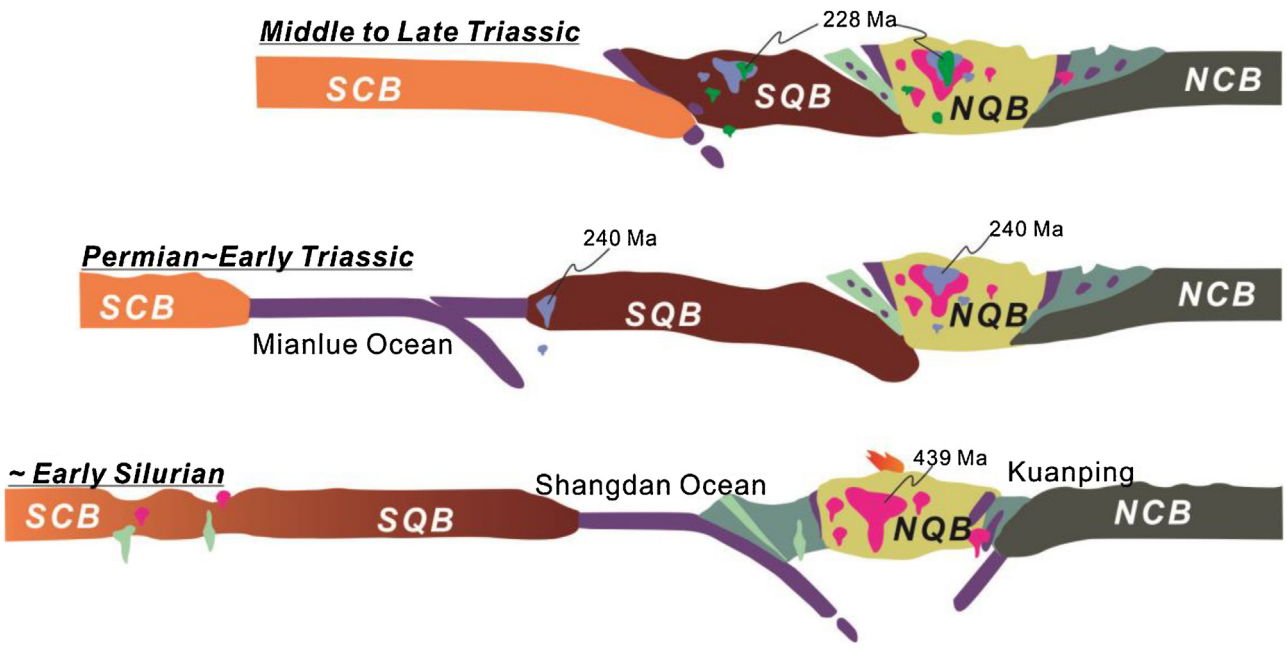

Fig. 7. Schematic time-space evolution diagram for the geotectonic setting of the Western Qinling (Modified after Dong et al., 2011; Wang et al., 2013; Yang et al., 2015a; Qiu et al., 2016b). SCB = South China block, NCB = North China block, SQB = South Qinling block, NQB = North Qinling block. See text for discussion.

calc-alkaline affinity. They show characteristics of moderate LREEs enrichments, slight HREEs depletions, and strong depletion of Nb, Ta, P and Ti, with negligible to slightly negative Eu anomalies. In addition, their features of high Rb/Zr and Ta/Nb and low K/Rb ratios indicates that they could possibly be syn-collision peraluminous intrusions derived from the hydrated bases of continental thrust sheets (Duggen et al., 2005; Wang et al., 2013; Dong and Santosh, 2016). We thus propose that the magmas, from which the of ca. 240 Ma biotite monzogranite and ca. 228 Ma monzogranite crystallized, were originated from the reworking of Paleoproterozoic ancient crust and partial melting of Neoproterozoic juvenile crust. The monzogranite could have undergone more significant source contamination, or more possible crustal assimilation than the precursor biotite monzogranite during their crystallization at ca. 228 Ma.

5.3. Tectonic implications for Western Qinling

The evolutionary history of the Western Qinling and its surrounding blocks holds important evidence to understand the tectonic process during assembly between the Tarim block, North China block, Qaidam block and South China block assemblies (Yang et al., 2015a; Wang et al., 2016a,b). Orogenic belts widely distributed recorded the history of plates convergence and orogenic processes (e.g., Deng et al., 2017; Zhang et al., 2017). The Dangchuan complex is located in the conjunction area of South Qinling block, North Qinling block and North China block, a key tectonic position which records the amalgamation from accretionary and collisional processes between these continental blocks along the Dabie, Qinling, Qilian and Kunlun Mountains from east to west (Zhang et al., 2015; Deng et al., 2015a; Liu et al., 2016). It has been well established that the Paleozoic Shangdan suture zone reflects the closure of the Shangdan ocean and multistage amalgamation of the South China block-South Qinling block to the North China block during the Paleozoic (Meng and Zhang, 2000; Yang et al., 2015b), and the Triassic A'nimaqing-Mainlue suture zone to the south represents the closure of a northern branch of the eastern Paeotethyan ocean which separated the South Qinling block from the South China block (Liu et al., 2011; Yang et al., 2015b).

Previous researches suggest that Silurian–Devonian plutons in the North Qinling block formed in either an island-arc setting along the Shangdan suture (Dong et al., 2011; Tang et al., 2016), or the southward subduction of Kuanping oceanic crust (Yu et al., 2015; Zhao et al., 2015; Cao et al., 2016; Li et al., 2017a), or a continental arc setting related to subduction along the Erlangping suture (e.g., Xue et al., 1996a,b; Ratschbacher et al., 2003). The precise timing of the subduction and collision during Triassic in Western Qinling between these continental blocks, however, are still widely disputed.

Tectonic setting and petrogenesis are intimately intertwined (Upadhyay and Raith, 2006; Chen and Santosh, 2014; Pirajno and Zhou, 2015). Our geochronological and geochemical data in this contribution thus suggests that the Dangchuan complex underwent an episodic growth from early Paleozoic to Triassic which probably documents the subduction and collision processes in the Western Qinling. The ca. 439 Ma zircon derived from the monzogranite could represent magmatism correlated to the persistent northward subduction of the Shangdan (Dong et al., 2011; Dong and Santosh, 2016; Tang et al., 2016) or southward subduction of Kuanping (Yu et al., 2015; Zhao et al., 2015; Cao et al., 2016; Li et al., 2017a) oceanic crust (Fig. 7). The negative $\varepsilon_{Hf}(t)$ value (−2.1) and corresponding calculated T_{DM2} (2.02 Ga) are also consistent to that of widespread coeval subduction-related granitic intrusions confined to the northern side of the Shangdan suture zone (Dong et al., 2011), especially within the North Qinling island-arc terrane (Qiu et al., 2015), including Caochuanpu granite (434 ± 10 Ma), Yanjiadian diorite (441 ± 10 Ma), Wangjiacha diorite (455 ± 1.7 Ma), Tangzang granitoid (455 ± 1.9 Ma), Honghuapu diorite (414 ± 1.5 Ma), and Wangdian porphyritic granodiorite (444.6 ± 7.8 Ma). A rift meanwhile developed within the northern South China block, which were covered by shale and siltstone to the south (Tang et al., 2016).

After the closure of Shandan ocean at ca. 400 Ma, the uplift and exhumation of the basement still occurred to the north, and the Mianlue basin developed at the northern margin of the South China

block due to the extension and subsidence to the south (Tang et al., 2015). The broadly coeval early Indosinian magmatism throughout Western Qinling and Eastern Kunlun defines a regionally similar geodynamic process related to the Paleotethys ocean and marks the consumption of the Paleotethys ocean at ca. 235 Ma by northward subduction (Yan et al., 2014). The ca. 240 Ma biotite monzogranite was emplaced during the northward subduction of the Mianlue oceanic crust beneath the South Qinling block. The collision between the South China block and united South Qinling-North Qinling blocks along the present Mianlue suture zone subsequently started after the consumption of the Mianlue oceanic crust at ca. 235 Ma (Qiu et al., 2015). The ca. 228 Ma monzogranite was emplaced probably through the escape structures cutting through the precursor ca. 439 Ma and ca. 240 Ma phases of Dangchuan complex during thecollisional process in a compressional setting. Numerous previous geochronological data have acknowledged the broadly Triassic magmatism throughout the Western Qinling (Dong et al., 2011; Wang et al., 2013). Three distinct stages of magmatism during the time intervals of 250–235 Ma (early subduction stage) and 228–190 Ma (later collision stage) (Qiu and Deng, 2016). The ca. 439 Ma inherited zircon and their hafnium isotopic composition indicate a tectonic regime switchover from the northward subduction of the Paleotethys ocean setting at ca. 240 Ma to a subsequent continent-continent collision setting at ca. 228 Ma. Moreover, some of the 250 235 Ma subdcution-related intrusive rocks are genetically related to early Triassic porphyry- and skarn-type copper and gold mineralization in Western Qinling, including Xiekeng, Dewulu, Laodou, and Jiangligou deposits (Qiu and Deng 2016 and references therein). The 228–215 Ma syn-collisional granitoids are genetically associated with porphyry molybdenum and tungsten mineralization including Wenquan, Jiangligou and Taiyangshan deposits probably due to their more contribution of the ancient crust during the source contamination, or more possible crustal assimilation during their crystallization (Qiu et al., 2016b; Wang et al., 2017; Li and Pirajno, 2017). The findings therefore provide us implications on the possibility of vast potential for copper and gold mineralization likely correlated to the northward subduction of the Paleotethys oceanic slab during the Early Triassic and molybdenum and gold mineralization possibly related to orogeny regionally.

6. Conclusion

The following conclusions can be made based on our new robust geochronological and geochemical data on zircons together with detailed petrological studies documented in this present contribution.

(1) The biotite monzogranite and monzogranite phases was emplaced at 239.8 ± 2.3 Ma and 227.8 ± 1.2 Ma, respectively. These are the first systematically identified Triassic granitic rocks of the Dangchuan intrusive complex, and are coeval with the Triassic magmatism throughout the Western Qinling.
(2) The 439 ± 6 Ma inherited zircon from monzogranite possibly documented precursor early Paleozoic magmatism associated to subduction of the ocean crust.
(3) The parental magmas of biotite monzogranite and monzogranite were originated from hybrid sources of both reworking of Paleoproterozoic ancient crust and partial melting of the Neoproterozoic juvenile crust. The more negative $\varepsilon_{Hf}(t)$ values of the monzogranite suggest more contribution of the ancient crust during the source contamination, or more possible crustal assimilation during their crystallization at ca. 228 Ma than precursor biotite monzogranite.
(4) The Dangchuan complex underwent an episodic growth documenting the tectonic regime switchover from early Paleozoic to Triassic. The ca. 439 Ma inherited zircon recorded the persistent subduction of the oceanic crust, the ca. 240 Ma biotite monzogranite emplaced during the northward subduction of the Mianlue oceanic crust beneath the South Qinling block, and the ca. 228 Ma monzogranite emplaced during the syn-collisional process in a compressional setting.

Acknowledgments

Constructive comments from Prof. Upadhyay Dewashish and two anonymous reviewers are greatly appreciated. We are very grateful to Editor-in-Chief Prof. Alexander Deutsch for quick handling and Dr. Li Tang at China University of Geosciences for thoughtful discussion. This research was financially supported by the National Natural Science Foundation of China (41403045), China Postdoctoral Science Foundation (2016M591221), State Key Laboratory for Mineral Deposits Research (2017-LAMD-K05), MLR Key Laboratory of Metallogeny and Mineral Assessment (ZS1707) and Key Laboratory of Western Mineral Resources and Geological Engineering of Ministry of Education at Chang'an University (310826171109).

References

Amelin, Y., Davis, W.J., 2005. Geochemical test for branching decay of 176Lu. Geochim. Cosmochim. Acta 69, 465–473.
Anderson, T., 2002. Correction of common lead in U–Pb analyses that do not report 204Pb. Chem. Geol. 192, 59–79.
Begemann, F., Ludwig, K.R., Lugmair, G.W., Min, K., Nyquist, L.E., Patchett, P.J., Renne, P.R., Shih, C.Y., Villa, I.M., Walker, R.J., 2001. Call for an improved set of decay constants for geochronological use. Geochim. Cosmochim. Acta 65, 111–121.
Belousova, E.A., Griffin, W.L., O'Reilly, S.Y., 2006. Zircon crystal morphology, trace element signatures and Hf isotope composition as a tool for petrogenetic modelling: examples from Eastern Australian granitoids. J. Petrol. 47, 329–353.
Bian, Q.T., Li, D.H., Pospelov, I., Yin, L.M., Li, H.S., Zhao, D.-S., Chang, C.F., Luo, X.Q., Upadhyay, S.L., Astrakhantsev, O., Chamov, N., 2004. Age, geochemistry and tectonic setting of Buqingshan ophiolites, North Qinghai-Tibet Plateau, China. J. Asian Earth Sci. 23, 577–596.
Blichert-Toft, J., Albarède, F., 1997. The Lu-Hf isotope geochemistry of chondrites and the evolution of the mantle–crust system. Earth Planet. Sci. Lett. 148, 243–258.
Cao, H.H., Li, S.Z., Zhao, S.J., Yu, S., Li, X.Y., Somerville, I.D., 2016. Detrital zircon geochronology of Neoproterozoic to early Paleozoic sedimentary rocks in the North Qinling Orogenic Belt: implications for the tectonic evolution of the Kuanping Ocean. Precambrian Res. 279, 1–16.
Chen, Y.J., Santosh, M., 2014. Triassic tectonics and mineral systems in the Qinling Orogen, China. Geol. J. 49 (4–5), 338–358.
Chu, Nan-Chin, Taylor, Rex N., Chavagnac, Valeírie, Nesbitt, Robert W., Boella, Rose M., Milton, J. Andrew, German, Christopher R., Bayon, Germain, Burton, Kevin, 2002. Isotope ratio analysis using multi-collector inductively coupled plasma mass spectrometry: an evaluation of isobaric interference corrections. J. Anal. At. Spectrom. 17, 1567–1574.
Corfu, F., Stott, G.M., 1993. Age and petrogenesis of two late Archean magmatic suites, northwestern Superior Province, Canada: zircon U–Pb and Lu–Hf isotopic relations. J. Petrol. 34, 817–838.
Corfu, F., Hanchar, J.M., Hoskin, P.W.O., Kinny, P., 2003. Atlas of zircon textures. Rev. Mineral. Geochem. 53, 469–495.
Deng, J., Wang, Q.F., 2016. Gold mineralization in China: metallogenic provinces, deposit types and tectonic framework. Gondwana Res. 36, 219–274.
Deng, J., Wang, Q.F., Li, G.J., Santosh, M., 2014a. Cenozoic tectono-magmatic and metallogenic processes in the Sanjiang region southwestern China. Earth Sci. Rev. 138, 268–299.
Deng, J., Wang, Q.F., Li, G.J., Li, C.S., Wang, C.M., 2014b. Tethys tectonic evolution and its bearing on the distribution of important mineral deposits in the Sanjiang regionn, SW China. Gondwana Res. 26, 419–437.
Deng, J., Wang, Q.F., Li, G.J., Hou, Z.Q., Jiang, C.Z., Danyushevsky, L., 2015a. Geology and genesis of the giant Beiya porphyry-skarn gold deposit northwestern Yangtze Block, China. Ore Geol. Rev. 70, 457–485.
Deng, J., Wang, Q.F., Li, G.J., Zhao, Y., 2015b. Structural control and genesis of the Oligocene Zhenyuan orogenic gold depositt, SW China. Ore Geol. Rev. 65, 42–54.
Deng, J., Wang, Q.F., Li, G.J., 2017. Tectonic evolution, superimposed orogeny, and composite metallogenic system in China. Gondwana Res., http://dx.doi.org/10.1016/j.gr.2017.02.005.
Dong, Y.P., Santosh, M., 2016. Tectonic architecture and multiple orogeny of the Qinling Orogenic Belt, Central China. Gondwana Res. 29, 1–40.

Dong, Y.P., Zhang, G.W., Neubauer, F., Liu, X.M., Genser, J., Hauzenberger, C., 2011. Tectonic evolution of the Qinling orogen, China: review and synthesis. J. Asian Earth Sci. 41 (3), 213–237.
Dong, Y.P., Yang, Z., Liu, X.M., Sun, S.S., Li, W., Cheng, B., Zhang, F.F., Zhang, X.N., He, D.F., Zhang, G.W., 2016. Mesozoic intracontinental orogeny in the Qinling Mountains, central China. Gondwana Res. 30, 144–158.
Elhlou, S., Belousova, E., Griffin, W.L., Pearson, N.J., O'Reilly, S.Y., 2006. Trace element and isotopic composition of GJ–red zircon standard by laser ablation. Geochim. Cosmochim. Acta 70, 158.
Goolaerts, A., Mattielli, N., de Jong, J., Weis, D., Scoates, J.S., 2004. Hf and Lu isotopic reference values for the zircon standard 91500 by MC-ICP-MS. Chem. Geol. 206, 1–9.
Griffin, W.L., Pearson, N.J., Belousova, E., Jackson, S.E., van Achterbegrh, E., O'Reilly, Suzanne Y., Shee, S.R., 2000. The Hf isotope composition of cratonic mantle: LAM-MC-ICPMS analysis of zircon megacrysts in kimberlites. Geochim. Cosmochim. Acta 64 (1), 133–147.
Griffin, W.L., Wang, X., Jackson, S.E., Pearson, N.J., O'Reilly, S.Y., Xu, X., Zhou, X.M., 2002. Zircon chemistry and magma mixing: SE China: in-situ analysis of Hf isotopes, Tonglu and Pingtan igneous complexes. Lithos 61, 237–269.
Jackson, S.E., Pearson, N.J., Griffin, W.L., Belousova, E.A., 2004. The application of laser ablation-inductively coupled plasma-mass spectrometry to in situ U–Pb zircon geochronology. Chem. Geol. 211, 47–69.
Jiang, Y.H., Jin, G.D., Liao, S.Y., Zhou, Q., Zhao, P., 2010. Geochemical and Sr–Nd–Hf isotopic constraints on the origin of late Triassic granitoids from the Qinling orogen, central China: implications for a continental arc to continent–continent collision. Lithos 117, 183–197.
Kinny, P.D., Maas, R., 2003. Lu–Hf and Sm–Nd isotope systems in zircon. In: Hanchar, J.M., Hoskin, P.W.O. (Eds.), Zircon. Rev. Mineral. Geochem., 53, pp. 327–341.
Li, N., Pirajno, F., 2017. Early Mesozoic Mo mineralization in the Qinling Orogen: an overview. Ore Geol. Rev. 81, 431–450.
Li, Y.J., Li, S.C., Yang, J.Q., Liu, J., Wen, Z.L., Yang, Z.M., 2005. The Disintergration of granite bodies in the Dangchuan area of Western Qinling: evidence from the isotopic dating ages. Bull. Mineral. Petrol. Geochem. 24, 114–120 (in Chinese with English abstract).
Li, S.Z., Kusky, T.M., Wang, L., Zhang, G.W., Lai, S.C., Liu, X.C., Dong, S.W., Zhao, G.C., 2007a. Collision leading to multiple-stage large-scale extrusion in the Qinling orogen: insights from the Mianlue suture. Gondwana Res. 12 (1–2), 121–143.
Li, Y.J., Gu, P.Y., Liu, J., Li, J.b., Bi, M.B., Yang, J.Q., Jiang, H.B., 2007b. Geochemistry of the Dangchuan granitic batholith in West Qinling. Northwest. Geol. 40 (1), 35–41 (in Chinese with English abstract).
Li, N., Chen, Y.J., Santosh, M., Pirajno, F., 2015a. Compositional polarity of Triassic granitoids in the Qinling orogen, China: implication for termination of the northernmost paleo-Tethys. Gondwana Res. 27, 244–257.
Li, X.W., Mo, X.X., Huang, X.F., Dong, G.C., Yu, X.H., Luo, M.F., Liu, Y.B., 2015b. U–Pb zircon geochronology, geochemical and Sr-Nd-Hf isotopic compositions of the Early Indosinian Tongren Pluton in West Qinling: petrogenesis and geodynamic implications. J. Asian Earth Sci. 97, 38–50.
Li, S.Z., Zhao, S.J., Yu, S., Cao, H.H., Li, X.Y., Guo, X.Y., Xiao, W.J., Lai, S.C., Yan, Z., Li, Z.H., Yu, S.Y., Zhang, J., Lan, H.Y., 2016. Proto-Tethys Ocean in East Asia (II): afinity and assembly of Early Paleozoic microcontinental blocks. Acta Petrol. Sin. 32 (9), 2628–2644 (in Chinese with English abstract).
Li, S.Z., Jahn, B.G., Zhao, S.J., Dai, L.M., Li, X.Y., Suo, Y.H., Guo, L.L., Wang, Y.M., Li, X.C., Lan, H.Y., Zhou, Z.Z., Zheng, Q.L., Wang, P.C., 2017a. Triassic southeastward subduction of North China Block to South China Block: insights from new geological, geophysical and geochemical data. Earth-Sci. Rev. 166, 270–285.
Li, S.Z., Zhao, S.J., Liu, X., Cao, H.H., Yu, S., Li, X.Y., Somerville, I., Yu, S.Y., Suo, Y.H., 2017b. Closure of the Proto-Tethys Ocean and Early Paleozoic amalgamation of microcontinental blocks in East Asia. Earth-Sci. Rev., http://dx.doi.org/10.1016/j.earscirev.2017.01.011.
in Chinese with English abstract)Liu, X.H., Deng, J., Sun, X.L., Liu, J.F., Sun, B.N., Kang, H.J., 2010. Molybdenite Re–Os dating and C-H-O-S isotopic characteristics of the Ganbahenao Mo–W deposit in Western Segment of North Qilian Mountains. J. Jilin Univ.: Earth Sci. Ed. 40, 845–851.
Liu, Y., Deng, J., Shi, G.H., Sun, X., Yang, L.Q., 2011. Geochemistry and petrogenesis of placer nephrite in Hetian Xinjiang, northwest China. Ore Geol. Rev. 41, 122–132.
Liu, Y., Deng, J., Shi, G.H., Sun, X., Yang, L.Q., 2012. Genesis of the Xuebaoding W-Sn-Be crystal deposits in Southwest China Evidence from fluid inclusions, stable isotopes and ore elements. Resour. Geol. 62, 159–173.
Liu, Y., Zhang, R.Q., Matuohuti, A., Wang, C., Zhang, S.P., Shen, C.H., Zhang, Z.Y., He, M.Y., Zhang, Y., Yang, X.D., 2016. Shrimp U-Pb zircon ages, mineral compositions and geochemistry of placer nephrite in the Yurungkash and Karakash rivers deposits West Kunlun, Xinjiang, Northwest China. Ore Geol. Rev. 72, 699–727.
Lizuka, T., Hirata, T., 2005. Improvements of precision and accuracy in in-situ Hf isotope microanalysis of zircon using the laser ablation-MC-ICPMS technique. Chem. Geol. 220, 121–137.
Ludwig, K.R., 2003. Isoplot v. 3.0: A Geochronological Toolkit for Microsoft Excel. Berkeley Geochronology Center Special Publication, pp. 1–70.
Luo, B.J., Zhang, H.F., Lü, X.B., 2012. U-Pb zircon dating, geochemical and Sr-Nd-Hf isotopic compositions of Early Indosinian intrusive rocks in West Qinling, central China: petrogenesis and tectonic implications. Contrib. Mineral. Petrol. 164, 551–569.
Meng, Q.R., Zhang, G.W., 2000. Geologic framework and tectonic evolution of the Qinling orogen, central China. Tectonophysics 323, 183–196.
Pirajno, F., Zhou, T.F., 2015. Intracontinental porphyry and porphyry-skarn mineral systems in Eastern China: scrutiny of a special case Made-in-China. Econ. Geol. 110, 603–629.
Qiu, K.F., Deng, J., 2016. Petrogenesis of granitoids in the Dewulu skarn copper deposit: implications for the evolution of the Paleotethys ocean and mineralization in Western Qinling, China. Ore Geol. Rev., http://dx.doi.org/10.1016/j.oregeorev.2016.09.027.
Qiu, K.F., Song, K.R., Song, Y.H., 2015. Magmatic-hydrothermal fluid evolution of the Wenquan porphyry molybdenum deposit in the north margin of the Western Qinling, China. Acta Petrol. Sin. 31, 3391–3404 (in Chinese with English abstract).
Qiu, K.F., Deng, J., Taylor, R.D., Song, K.R., Song, Y.H., Li, Q.Z., Goldfarb, J.R., 2016a. Paleozoic magmatism and porphyry Cu-mineralization in an evolving tectonic setting in the North Qilian Orogenic Belt, NW China. J. Asian Earth Sci. 122, 20–40.
Qiu, K.F., Taylor, R.D., Song, Y.H., Yu, H.C., Song, K.R., Li, N., 2016b. Geologic and geochemical insights into the formation of the Taiyangshan porphyry copper-molybdenum deposit Western Qinling Orogenic Belt, China. Gondwana Res. 35, 40–58.
Ratschbacher, L., Hacker, B.R., Calvert, A., Webb, L.E., Grimmer, J.C., McWilliams, M.O., Ireland, T., Dong, S.W., Hu, J.M., 2003. Tectonics of the Qinling (central China): tectonostratigraphy geochronology, and deformation history. Tectonophysics 366, 1–53.
Schellart, W.P., Rawlinson, N., 2010. Convergent plate margin dynamics: new perspectives from structural geology, geophysics and geodynamic modelling. Tectonophysics 483, 4–9.
Scherer, E., Münker, C., Mezger, K., 2001. Calibration of the lutetium-hafnium clock. Science 293, 683–687.
Soderlund, Ulf, Patchett, P. Jonathan, Vervoort, Jeffrey D., Isachsen, Clark E., 2004. The 176Lu decay constant determined by Lu–Hf and U–Pb isotope systematics of Precambrian mafic intrusions. Earth Planet. Sci. Lett. 219, 311–324.
Tang, L., Santosh, M., Dong, Y.P., 2015. Tectonic evolution of a complex orogenic system: evidence from the northern Qinling belt, central China. J. Asian Earth Sci. 113, 544–559.
Tang, L., Santosh, M., Dong, Y.P., Tsunogae, T., Zhang, S.T., Cao, H.W., 2016. Early Paleozoic tectonic evolution of the North Qinling orogenic belt Evidence from geochemistry, phase equilibrium modeling and geochronology of metamorphosed mafic rocks from the Songshugou ophiolite. Gondwana Res. 30, 48–64.
Upadhyay, D., Raith, M.M., 2006. Intrusion age, geochemistry and metamorphic conditions of a quartz-monzosyenite intrusion at the craton–Eastern Ghats Belt contact near Jojuru, India. Gondwana Res. 10, 267–276.
Vervoort, J.D., Blichert-Toft, J., 1999. Evolution of the depleted mantle: Hf isotope evidence from juvenile rocks through time. Geochim. Cosmochim. Acta 63, 533–556.
Wang, J., Zhang, H.F., Xu, W.C., Cai, H.M., 2008. Petrogenesis of granites from Dangchuan area in West Qinling Orogenic Belt and its tectonic implication. Earth Sci.: J. China Univ. Geosci. 33, 474–486.
Wang, X.X., Wang, T., Zhang, C.L., 2013. Neoproterozoic, paleozoic, and mesozoic granitoid magmatism in the Qinling orogen, China: constraints on orogenic process. J. Asian Earth Sci. 72, 129–151.
Wang, C.M., Deng, J., Carranza, E.J.M., Santosh, M., 2014a. Tin metallogenesis associated with granitoids in the southwest Sanjiang Tethyan Domain: nature, types, and tectonic setting. Gondwana Res. 26, 576–593.
Wang, Q.F., Deng, J., Li, C.S., Li, G.J., Yu, L., Qiao, L., 2014b. The boundary between the Simao and Yangtze blocks and their locations in Gondwana and Rodinia: constraints from detrital and inherited zircons. Gondwana Res. 26, 438–448.
Wang, Y.H., Xue, C.J., Wang, J.P., Peng, R.M., Yang, J.T., Zhang, F.F., Zhao, Z.N., Zhao, Y.J., 2015. Petrogenesis of magmatism in the Yandong region of Eastern Tianshan, Xinjiang: geochemical, geochronological and Hf isotope Constraints. Int. Geol. Rev. 57 (9–10), 1130–1151.
Wang, H., Feng, C.Y., Li, D.X., Li, C., Ding, T.Z., Liao, F.Z., 2016a. Geology, geochronology and geochemistry of the Saishitang Cu deposit, East Kunlun Mountains, NW China: constraints on ore genesis and tectonic setting. Ore Geol. Rev. 72, 43–59.
Wang, Y.H., Xue, C.J., Liu, J.J., Zhang, F.F., 2016b. Geological, geochronological, geochemical, and Sr–Nd–O–Hf isotopic constraints on origins of intrusions associated with the Baishan porphyry Mo deposit in eastern Tianshan, NW China. Miner. Deposita 51, 953–969.
Wang, C.M., Deng, J., Bagas, L., Wang, Q., 2017. Zircon Hf-isotopic mapping for understanding crustal architecture and metallogenesis in the Eastern Qinling Orogen. Gondwana Res., http://dx.doi.org/10.1016/j.gr.2017.04.008.
Wen, Z.L., Xu, X.Y., Zhao, R.F., Wang, F., Hu, W., 2008. Geologic and geochemical features of Devonian Granites in Dangchuan area, Western Qinling, and its tectonic significance. Geol. Rev. 54, 827–836.
Wu, F.Y., Yang, Y.H., Xie, L.W., Yang, J.H., Xu, P., 2006. Hf isotopic compositions of the standard zircons and baddeleyites used in U–Pb geochronology. Chem. Geol. 234, 105–126.
Yan, Z., Guo, X., Fu, C., Aitchison, J., Wang, Z., Li, J., 2014. Detrital heavy mineral constraints on the Triassic tectonic evolution of the West Qinling Terrane, NW China: implications for understanding subduction of the Paleotethyan Ocean. J. Geol. 122, 591–608.
Yang, L.Q., Deng, J., Dilek, Y., Qiu, K.F., Ji, X.Z., Li, N., Taylor, R.D., Yu, J.Y., 2015a. Structure, geochronology, and petrogenesis of the Late Triassic Puziba granitoid dikes in the Mianlue suture zone Qinling orogen, China. Geol. Soc. Am. Bull. 11, 1831–1854.

Yang, L.Q., Deng, J., Qiu, K.F., Ji, X.Z., Santosh, M., Song, K.R., Song, Y.H., Geng, J.Z., Zhang, C., Hua, B., 2015b. Magma mixing and crust-mantle interaction in the Triassic monzogranites of Bikou Terrane, central China: constraints from petrology, geochemistry, and zircon U-Pb-Hf isotopic systematics. J. Asian Earth Sci. 98, 320–341.

Yang, L.Q., Deng, J., Wang, Z.L., Guo, L.N., Li, R.H., Groves David, I., Danyushevsky Leonid, V., Zhang, C., Zheng, X.L., Zhao, H., 2016. Relationships between gold and pyrite at the Xincheng Gold Deposit Jiaodong Peninsula, China: implications for gold source and deposition in a Brittle Epizonal Environment. Econ. Geol. 111, 105–126.

Yu, S., Li, S.Z., Zhao, S.J., Cao, H.H., Suo, Y.H., 2015. Long history of a Grenville orogen relic-the North Qinling terrane: evolution of the Qinling orogenic belt from Rodinia to Gondwana. Precambrian Res. 271, 98–117.

Zhang, G.W., Meng, Q.R., Lai, S.C., 1995. Tectonics and structure of the Qinling Orogenic belt. Sci. China Ser. B 38, 1379–1394 (in Chinese).

Zhang, L.Y., Ding, L., Pullen, A., Xu, Q., Liu, D.L., Cai, F.L., Yue, Y.H., Lai, Q.Z., Shi, R.D., Ducea, M.N., Kapp, P., Chapman, A., 2014. Age and geochemistry of western Hoh-Xil-Songpan-Ganzi granitoids, northern Tibet: implications for the Mesozoic closure of the Paleo-Tethys ocean. Lithos 190–191, 328–348.

Zhang, J.Q., Li, S.R., Santosh, M., Li, Q., Niu, S.D., Li, Z.D., Zhang, X.G., Jia, L.B., 2015. Timing and origin of Mesozoic magmatism and metallogeny in the Wutai-Hengshan region: implications for destruction of the North China Craton. J. Asian Earth Sci. 113 (2), 677–694.

Zhang, R.Q., Lu, J.J., Lehmann, B., Li, C.Y., Li, G.L., Zhang, L.P., Guo, J., Sun, W.D., 2017. Combined zircon and cassiterite U-Pb dating of the Piaotang granite-related tungsten-tin deposit, southern Jiangxi tungsten district, China. Ore Geol. Rev. 82, 268–284.

Zhao, S.J., Li, S.Z., Liu, X., Santosh, M., Somerville, I.D., Cao, H.H., Yu, S., Zhang, Z., Guo, L.L., 2015. The northern boundary of the Proto-Tethys Ocean: constraints from structural analysis and U–Pb zircon geochronology of the North Qinling Terrane. J. Asian Earth Sci. 2, 560–574.